

Single-Phase Liquid Flow in Minichannels and Microchannels

3

Satish G. Kandlikar

Mechanical Engineering Department, Rochester Institute of Technology, Rochester, NY, USA

3.1 Introduction

3.1.1 Fundamental issues in liquid flow at microscale

Microchannels are used in a variety of devices incorporating single-phase liquid flow. The early applications involved micromachined devices such as micro-pumps, microvalves, and microsensors. This was followed by a thrust in the biological and life sciences with a need for analyzing biological materials, such as proteins, DNA, cells, embryos, and chemical reagents. The field of micromixers further received attention with developments in microreactors, where two chemical species are mixed prior to introducing them into a reaction chamber. The high flux heat dissipation from high-speed microprocessors provided the impetus for studies on heat transfer in microchannels.

The developments in the microelectromechanical devices naturally require heat removal systems that are equally small. The cooling of mirrors employed in high-power laser systems involves cooling systems that cover very small footprints. Advances in biomedical and genetic engineering require controlled fluid transport and its precise thermal control in passages with dimensions of several micrometers. A proper understanding of fluid flow and heat transfer in these microscale systems is therefore essential for their design and operation.

In dealing with liquid flows in minichannels and microchannels in the absence of any wall surface effects, such as the electrokinetic or electroosmotic forces (covered in Chapter 4), the flow is not expected to experience any fundamental changes from the continuum approximation employed in macrofluidic applications. [Gad-el-Hak \(1999\)](#) argued that liquids such as water should be treated as continuous media, with the results obtained from classical theory being applicable in channels larger than $1 \mu\text{m}$. However, there remain a number of unresolved

issues that require further study. The main areas of current research are summarized below:

1. Experimental validation of the laminar and turbulent flow transport equations: the laminar flow friction factor and heat transfer equations derived from theoretical considerations are expected to hold in microchannel applications in the absence of any changes in the transport processes or any new physical phenomena. Although explicit equations and experiments for mass transfer are not covered, the conclusions reached for the momentum and heat transfer are expected to be applicable to mass transport processes as well.
2. Verification of the laminar-to-turbulent flow transition at microscale: experimental evidence in this regard needs to be critically evaluated.
3. The effect of large relative roughness values on the flow: large values of relative roughness are more commonly encountered in microchannels. Their effect on the laminar-to-turbulent transition, friction factors, and heat transfer needs to be investigated.
4. Verification of empirical constants derived from macroscale experiments: a number of constants (such as for losses due to flow area changes, bends, etc.) whose values are derived from macroscale fluid flow experiments need to be verified for microscale applications.

This chapter will be devoted to answering the above questions on the basis of the evidence available in the literature.

3.1.2 Need for smaller flow passages

The flow passage dimensions in convective heat transfer applications have been shifting toward smaller dimensions for the following three main reasons:

1. Heat transfer enhancement.
2. Increased heat flux dissipation in microelectronic devices.
3. Emergence of microscale devices that require cooling.

Employing smaller channel dimensions results in higher heat transfer performance, although this is accompanied by a higher pressure drop per unit length. The higher volumetric heat transfer densities require advanced manufacturing techniques and lead to more complex manifold designs. An optimum balance for each application leads to different channel dimensions. For example, in the refrigeration industry, the use of microfin tubes of 6–8 mm diameter has replaced the plain tubes of larger diameters. In automotive applications, the passage dimensions for radiators and evaporators have approached a 1 mm threshold as a balance between the pumping power, heat transfer, and cleanliness constraints imposed by the overall system.

Microelectronic devices, including a variety of applications such as PCs, servers, laser diodes, and RF devices, are constantly pushing the heat flux density requirements to higher levels. What seemed to be an impossibly high limit of 200 W/cm^2 of heat dissipation in 1993 now seems to be a feasible target. The challenge for the coming decade is on the order of $600\text{--}1000 \text{ W/cm}^2$. The available temperature

differences are becoming smaller, in some cases as low as only a few degrees Celsius with external copper heat sinks. These high levels of heat dissipation require a dramatic reduction in the channel dimensions, matched with suitable coolant loop systems to facilitate the fluid movement away from the heat source.

A cooling system for a microscale device might require cooling channels of a few tens of micrometers as compared to more conventional-size channels with 1–3 mm flow passage dimensions. In addition, several such units may be clustered together and a secondary cooling loop may be employed to remove the heat with a conventional cooling system. [Figure 3.1](#) shows a schematic of a microchannel cooling system configuration for cooling a server application. The combination of (i) the microchannel heat exchangers, mounted directly on the chip or in the heat sink that is bonded to the chip; (ii) the water-cooled cold plates with minichannel or microchannel flow passages; and (iii) the auxiliary localized cooling systems will be able to address the cooling needs of the high-end servers. The cooling system is integrated with the building HVAC system, as described by [Kandlikar \(2005\)](#).

A schematic of direct liquid cooling of a multichip module or a heat sink is shown in [Figure 3.2](#). The liquid flows through the cold plates, which are attached to a substrate cap. In advanced designs, direct cooling of chips is accomplished by circulating water, a water–antifreeze mixture, oil, or a dielectric fluid such as

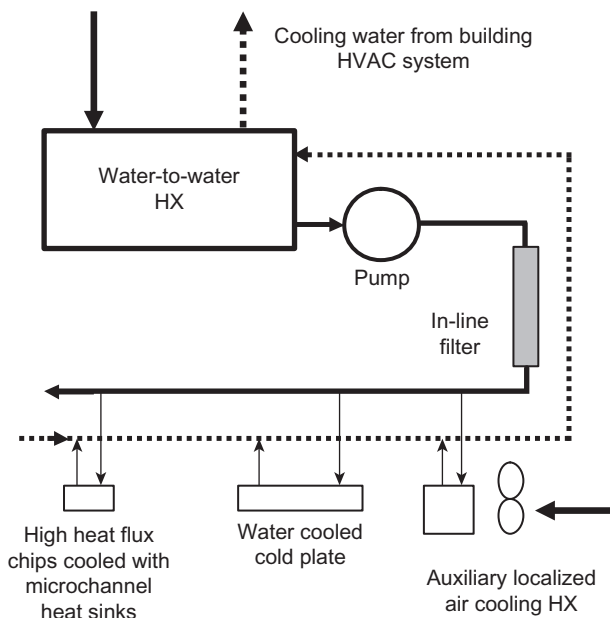
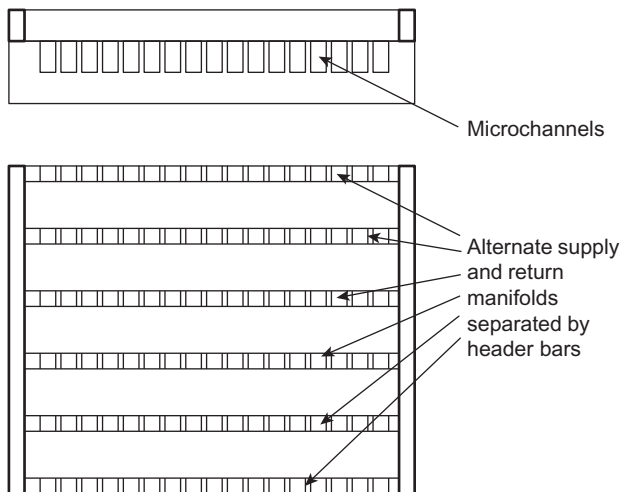


FIGURE 3.1

Schematic of a cluster of servers with high heat flux chips cooled with microchannel heat sinks, cold plates, and localized air cooling integrated with a secondary chilled water loop from the building HVAC system.

Source: From [Kandlikar \(2005\)](#).

**FIGURE 3.2**

Schematic of a microchannel cooling arrangement on a chip or a heat sink with alternate supply and return manifolds created by header bars, a design originally proposed by Tuckerman (1984).

FC-72, FC-77, or FC-87 through microchannels that are fabricated on the chip surface. Copper heat sinks with integrated microchannels and minichannels are expected to dominate heat sink applications.

3.2 Pressure drop in single-phase liquid flow

3.2.1 Basic pressure drop relations

One-dimensional flow of an incompressible fluid in a smooth circular pipe forms the basis for the pressure drop analysis in internal flows. The following equations are readily derived based on the continuum assumption for Newtonian liquid flows in minichannels and microchannels.

Considering the equilibrium of a fluid element of length dx in a pipe of diameter D , the force due to pressure difference dp is balanced by the frictional force due to shear stress τ_w at the wall.

$$\left(\frac{\pi}{4}D^2\right)dp = (\pi D dx)\tau_w \quad (3.1)$$

The pressure gradient and the wall shear stress are thus related by the following equation:

$$\frac{dp}{dx} = \frac{4\tau_w}{D} \quad (3.2)$$

For Newtonian fluids, the wall shear stress τ_w is expressed in terms of the velocity gradient at the wall:

$$\tau_w = \mu \frac{du}{dy} \Big|_w \quad (3.3)$$

where μ is the dynamic viscosity. The Fanning friction factor f is used in heat transfer literature because of its ability to represent the momentum transfer process of fluid flow in a manner consistent with the heat and mass transfer process representations:

$$f = \frac{\tau_w}{(1/2)\rho u_m^2} \quad (3.4)$$

where u_m is the mean flow velocity in the channel.

The frictional pressure drop Δp over a length L is obtained from Eqs. (3.2) and (3.4), respectively:

$$\Delta p = \frac{2f\rho u_m^2 L}{D} \quad (3.5)$$

The Fanning friction factor f in Eq. (3.5) depends on the flow conditions, the channel wall geometry, and surface conditions:

1. laminar or turbulent flow,
2. flow-channel geometry,
3. fully developed or developing flow,
4. smooth or rough walls.

For noncircular flow channels, the D in Eq. (3.5) is replaced by the hydraulic diameter D_h , represented by the following equation.

$$D_h = \frac{4A_c}{P_w} \quad (3.6)$$

where A_c is the flow-channel cross-sectional area and P_w is the wetted perimeter. For a rectangular channel of sides a and b , D_h is given by

$$D_h = \frac{4ab}{2(a+b)} = \frac{2ab}{(a+b)} \quad (3.7)$$

3.2.2 Fully developed laminar flow

The velocity gradient at the channel wall can be readily calculated from the well-known *Hagen–Poiseuille* parabolic velocity profile for the fully developed laminar flow in a circular pipe. Using this velocity profile, τ_w and f are obtained from Eqs. (3.3) and (3.4). The result for friction factor f is presented in the following form:

$$f = \frac{Po}{Re} \quad (3.8)$$

where Po is the Poiseuille number, ($Po = f Re$), which depends on the flow-channel geometry. Table 3.1 gives the $f Re$ product and the constant Nusselt

number (Nu) in the fully developed laminar flow region for different duct shapes, as derived from [Kakac et al. \(1987\)](#).

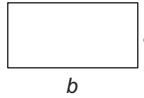
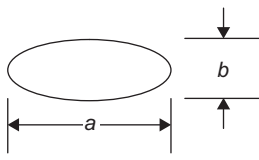
It can be seen that for a circular pipe,

$$Po = fRe = 16 \quad (3.9)$$

[Shah and London \(1978\)](#) provided the following equation for a rectangular channel with short side a and long side b , and a channel aspect ratio defined as $\alpha_c = a/b$.

$$fRe = 24(1 - 1.3553\alpha_c + 1.9467\alpha_c^2 - 1.7012\alpha_c^3 + 0.9564\alpha_c^4 - 0.2537\alpha_c^5) \quad (3.10)$$

Table 3.1 Fanning Friction Factor and Nusselt Number for Fully Developed Laminar Flow in Ducts, Derived from [Kakac et al. \(1987\)](#)

Duct Shape		Nu_H	Nu_T	$Po = fRe$	
	Circular	4.36	3.66	16	
	Flat channel	8.24	7.54	24	
	Rectangular, aspect ratio, $b/a =$	1 2 3 4 6 8 ∞	3.61 4.13 4.79 5.33 6.05 6.49 8.24	2.98 3.39 3.96 4.44 5.14 5.60 7.54	14.23 15.55 17.09 18.23 19.70 20.58 24.00
	Hexagon	4.00	3.34	15.05	
	Isosceles triangle, apex angle $\theta =$	10° 30° 60° 90° 120°	2.45 2.91 3.11 2.98 2.68	1.61 2.26 2.47 2.34 2.00	12.47 13.07 13.33 13.15 12.74
	Ellipse, major/minor axis $a/b =$	1 2 4 8 16	4.36 4.56 4.88 5.09 5.18	3.66 3.74 3.79 3.72 3.65	16.00 16.82 18.24 19.15 19.54

$$Nu = hD_f/k, Re = \rho u_m D_f / \mu$$

Nu_H — Nu under a constant heat flux boundary condition, constant axial heat flux, and uniform circumferential temperature.

Nu_T — Nu under a constant wall temperature boundary condition.

f —friction factor.

3.2.3 Developing laminar flow

As flow enters a duct, the velocity profile begins to develop along its length, ultimately reaching the fully developed Hagen–Poiseuille velocity profile. Almost all the analyses available in the literature consider a uniform velocity condition at the inlet. The length of the hydrodynamic developing region L_h is given by the following well-accepted equation:

$$\frac{L_h}{D_h} = 0.05Re \quad (3.11)$$

Since the pressure gradients found in small-diameter channels are quite high, the flow lengths are generally kept low. In many applications, the length of channel in the developing region therefore forms a major portion of the flow length through a microchannel. To account for the developing region, the pressure drop equations are presented in terms of an apparent friction factor.

Apparent friction factor f_{app} accounts for the pressure drop due to friction and the developing region effects. It represents an average value of the friction factor over the flow length between the entrance section and the location under consideration. Thus the pressure drop in a channel of hydraulic diameter D_h over a length x from the entrance is expressed as:

$$\Delta p = \frac{2f_{app}\rho u_m^2 x}{D_h} \quad (3.12)$$

The difference between the apparent friction factor over a length x and the fully developed friction factor f is expressed in terms of an incremental pressure defect $K(x)$:

$$K(x) = (f_{app} - f) \frac{4x}{D_h} \quad (3.13)$$

For $x > L_h$ the incremental pressure defect attains a constant value $K(\infty)$, known as *Hagenbach's factor*.

Combining Eqs. (3.12) and (3.13), the pressure drop can be expressed in terms of the incremental pressure drop:

$$\Delta p = \frac{2(f_{app}Re)\mu u_m x}{D_h^2} = \frac{2(fRe)\mu u_m x}{D_h^2} + K(x) \frac{\rho u_m^2}{2} \quad (3.14)$$

For a circular tube, Hornbeck (1964) obtained the axial velocity distribution and pressure drop in a nondimensional form. He estimated the fully developed region to begin at $x^+ = 0.0565$, with a value of $K(\infty) = 1.28$ for a

circular duct. [Chen \(1972\)](#) proposed the following equation for $K(\infty)$ for the circular geometry:

$$K(\infty) = 1.20 + \frac{38}{Re} \quad (3.15)$$

The nondimensionalized length x^+ is given by:

$$x^+ = \frac{x/D_h}{Re} \quad (3.16)$$

[Shah and London \(1978\)](#) showed that the frictional pressure drop in the developing region of a circular duct obtained by [Hornbeck \(1964\)](#) can be accurately described by the following equation:

$$\frac{\Delta p}{(1/2)\rho u_m^2} = 13.74(x^+)^{1/2} + \frac{1.25 + 64x^+ - 13.74(x^+)^{1/2}}{1 + 0.00021(x^+)^{-2}} \quad (3.17)$$

Rectangular geometries are of particular interest in microfluidics applications. [Shah and London \(1978\)](#) and [Kakac et al. \(1987\)](#) presented comprehensive summaries of the available literature. [Phillips \(1987\)](#) reviewed the available information, including that from [Curr et al. \(1972\)](#), and compiled the results for the apparent friction factor in a rectangular duct as shown in [Figure 3.3](#). It can be seen that fully developed flow is attained at different x^+ values, with low-aspect-ratio ducts

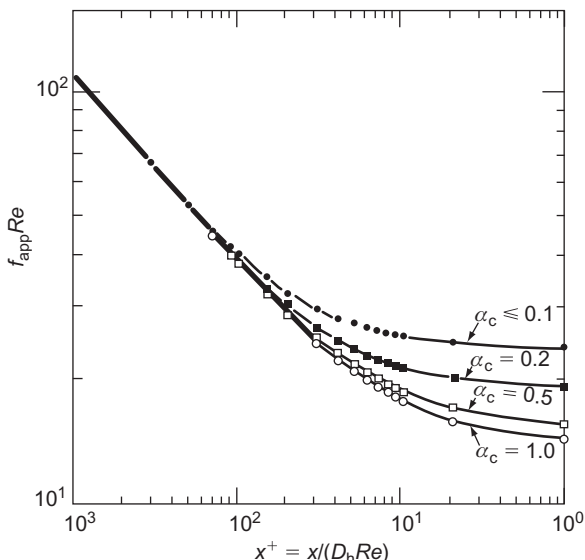


FIGURE 3.3

Apparent friction factors for rectangular ducts in the developing region for different aspect ratios ($\alpha = 1/\alpha_c$).

Source: From [Phillips \(1987\)](#).

reaching it earlier. The constant 0.05 in Eq. (3.11) is modified to around 1 ($x^+ = 10^0$) for fully developed value in rectangular ducts, as seen in Figure 3.3. Table 3.2, derived from Phillips (1987), gives the values of the apparent friction factor in tabular form.

For other channel aspect ratios, a linear interpolation is suggested. Alternatively, use the curve-fit equations provided in Appendix A.

The results for the fully developed friction factors and Hagenbach's factors in trapezoidal channels are reported by Kakac et al. (1987). By considering the rectangular channels as a subset of the trapezoidal geometry, Steinke and Kandlikar (2005a) obtained the following curve-fit equation for the Hagenbach's factor for rectangular channels:

$$K(\infty) = 0.6796 + 1.2197\alpha_c + 3.3089\alpha_c^2 - 9.5921\alpha_c^3 + 8.9089\alpha_c^4 - 2.9959\alpha_c^5 \quad (3.18)$$

Table 3.2 Laminar Flow Friction Factor in the Entrance Region of Rectangular Ducts (Phillips, 1987)

$x^+ = (x/D_h)/Re$	$f_{app}Re$			
	$\alpha_c = 1.0$	$\alpha_c = 0.5$	$\alpha_c = 0.2$	$\alpha_c \leq 0.1$ $\alpha_c \geq 10$
0	142.0	142.0	142.0	287.0
0.001	111.0	111.0	111.0	112.0
0.003	66.0	66.0	66.1	67.5
0.005	51.8	51.8	52.5	53.0
0.007	44.6	44.6	45.3	46.2
0.009	39.9	40.0	40.6	42.1
0.01	38.0	38.2	38.9	40.4
0.015	32.1	32.5	33.3	35.6
0.02	28.6	29.1	30.2	32.4
0.03	24.6	25.3	26.7	29.7
0.04	22.4	23.2	24.9	28.2
0.05	21.0	21.8	23.7	27.4
0.06	20.0	20.8	22.9	26.8
0.07	19.3	20.1	22.4	26.4
0.08	18.7	19.6	22.0	26.1
0.09	18.2	19.1	21.7	25.8
0.10	17.8	18.8	21.4	25.6
0.20	15.8	17.0	20.1	24.7
> 1.0	14.2	15.5	19.1	24.0

For intermediate values use the curve-fit equations provided in Appendix A at the end of the chapter.

The analysis presented in this section assumes a uniform velocity profile at the entrance of the channel. In many microfluidic applications, the channels have the manifold surfaces flush with the two opposing channel surfaces. The effect of such an arrangement was investigated numerically by [Gamrat et al. \(2004\)](#). They showed that the resulting apparent friction factors in the entrance region could be up to 50% lower than the theoretical predictions.

3.2.4 Fully developed and developing turbulent flow

A number of correlations with comparable accuracies are available in literature for fully developed turbulent flow in smooth channels. The following equation by Blasius is used extensively:

$$f = 0.0791 Re^{-0.025} \quad (3.19)$$

A more accurate equation was presented by [Phillips \(1987\)](#) to cover both the developing and fully developed flow regions. He presented the Fanning friction factor for a circular tube in terms of the following equation:

$$f_{\text{app}} = A Re^B \quad (3.20)$$

where

$$A = 0.09290 + \frac{1.01612}{x/D_h} \quad (3.21)$$

$$B = 0.26800 - \frac{0.32930}{x/D_h} \quad (3.22)$$

For rectangular channel geometries, Re is replaced with the laminar-equivalent Reynolds number ([Jones, 1976](#)) given by:

$$Re^* = \frac{\rho u_m D_{le}}{\mu} = \frac{\rho u_m [(2/3) + (11/24)(1/\alpha_c)(2 - 1/\alpha_c)]D_h}{\mu} \quad (3.23)$$

where D_{le} is the laminar-equivalent diameter given by the term in the brackets in Eq. (3.23).

3.3 Total pressure drop in a microchannel heat exchanger

3.3.1 Entrance and exit loss coefficients

An earnest interest in microchannel flows began with the pioneering work on direct chip cooling with water by [Tuckerman and Pease \(1981\)](#). Recently, a number of investigators including [Li et al. \(2000\)](#), [Celata et al. \(2002\)](#), and [Steinke and Kandlikar \(2005a\)](#) critically evaluated the available literature and presented explanations for the large deviations from classical theory reported by some of the researchers.

A schematic representation of the pressure drop experiments conducted by the researchers is shown in [Figure 3.4](#). Since measuring the local pressure along the flow is difficult in microchannels, researchers have generally measured the pressure drop across the inlet and outlet manifolds. The resulting pressure drop measurement represents the combined effect of the losses in the bends, entrance and exit losses, developing region effects, and core frictional losses. Thus, the measured pressure drop is the sum of these components ([Phillips, 1987](#)):

$$\Delta p = \frac{\rho u_m^2}{2} \left[(A_c/A_p)^2 (2 K_{90}) + (K_c + K_e) + \frac{4f_{app}L}{D_h} \right] \quad (3.24)$$

where A_c and A_p are the total channel area and the total plenum cross-sectional area, K_{90} , is the loss coefficient at the 90-degree bends, K_c and K_e represent the contraction and expansion loss coefficients due to area changes, and f_{app} includes the combined effects of frictional losses and the additional losses in the developing flow region.

[Costaschuk et al. \(2007\)](#) measured pressure drop along a 91.3 μm -deep and 1161.5 μm -wide aluminum microchannel with a hydraulic diameter of 169 μm . They used 27 μm -diameter pressure ports along the flow length. The ports were

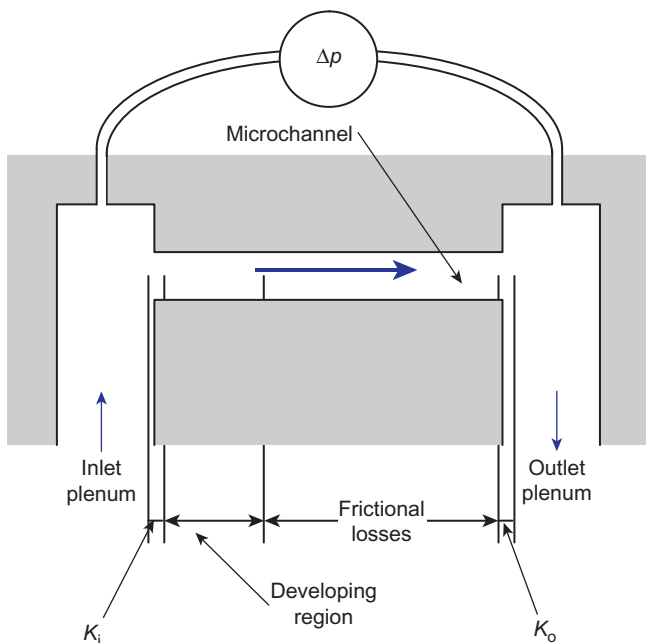


FIGURE 3.4

Schematic representation of the experiments employed by researchers for pressure drop measurements in microchannels.

Source: From [Steinke and Kandlikar \(2005a\)](#).

closer together near the entrance to capture the entrance region effect. They also measured the inlet and outlet pressure in the manifold. They noted that the fully developed laminar friction factor for the tested rectangular microchannel with an aspect ratio of 0.0786 was 86.85, while the theoretical value is 86.39. The Haaland equation was found to predict their turbulent data well. The entrance and exit loss coefficients of 0.42 and 1.46, respectively, in the turbulent flow were in agreement with the macroscale values. However, the equivalent lengths for inlet and exit regions in microscale were considerably lower, as given by the following equations in the laminar region:

$$\frac{L_{\text{eq,inlet}}}{D_h} = 0.026Re - 10.7 \quad (3.25)$$

$$\frac{L_{\text{eq,outlet}}}{D_h} = 0.021Re + 8.11 \quad (3.26)$$

In turbulent flow, the equivalent L_{eq}/D_h ratios for inlet and outlet sections were 14.7 and 38, respectively. The entrance region lengths in the laminar flow were found to be about half of the macroscale values.

[Szewczyk \(2008\)](#) conducted experiments with circular capillary tubes of 327.8 and 280.6 μm and obtained the sum of the entrance and exit loss coefficients. For a sharp-edged orifice, the total loss coefficient was 2.25 in the laminar flow and 1.45 in the turbulent flow. The rounding of the inlet and outlet edges of the capillaries resulted in an increase in the critical Reynolds number and a decrease in the minor losses in the turbulent flow. The minor losses were not affected in the laminar region.

[Phillips \(1987\)](#) studied these losses and recommended that K_{90} be approximately 1.2. [Xiong and Chung \(2007\)](#) obtained the loss coefficients during miter bend. They found it to be 1.1 in the laminar region. They recommended additional experiments to determine the Reynolds number and channel size effects.

The above results from [Costaschuk et al. \(2007\)](#) and [Szewczyk \(2008\)](#) clearly indicate that the entrance and exit loss coefficients and the entrance region lengths are affected by the microscale. The scale effect should not come as a surprise since values for the macroscale have been obtained empirically from measurements. A detailed experimental study covering different entrance and exit conditions for rectangular microchannels of different aspect ratios and other geometries is warranted. Until such experiments are available, the empirical values given by [Kays and London \(1984\)](#) for macroscale application are recommended as described below.

The contraction and exit losses can be read from [Figure 3.5](#), derived from [Kays and London \(1984\)](#) and [Phillips \(1990\)](#). [Figure 3.5A](#) is applicable to the low-aspect-ratio channels, $\alpha_c < 0.1$, and [Figure 3.5B](#) is for $0.1 \leq \alpha_c \leq 1.0$.

[Equation \(3.24\)](#) can also be written in terms of the fully developed friction factor f and the pressure drop defect $K(x)$:

$$\Delta p = \frac{\rho u_m^2}{2} \left[(A_c/A_p)^2 (2K_{90}) + (K_c + K_e) + \frac{4fL}{D_h} + K(x) \right] \quad (3.27)$$

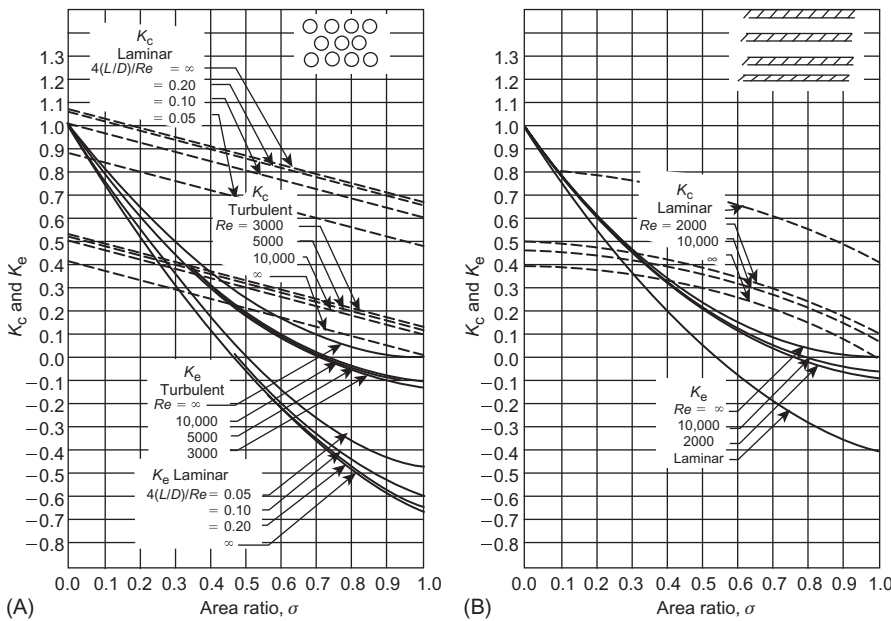


FIGURE 3.5

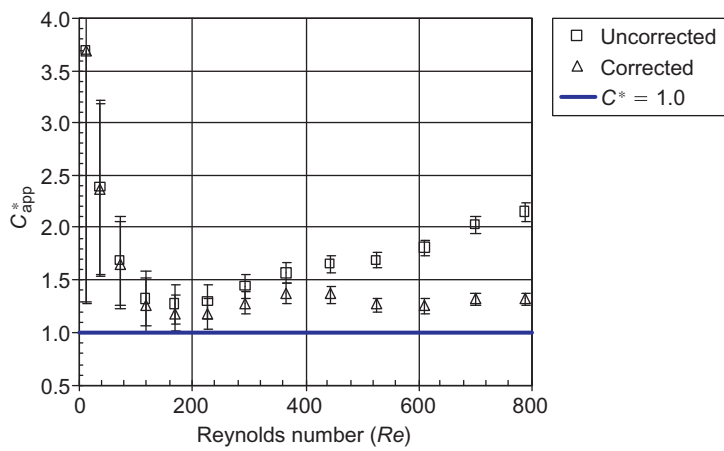
Contraction and expansion loss coefficients for flow between inlet and outlet manifolds and the microchannels: (A) $\alpha_c < 0.1$; and (B) $0.1 \leq \alpha_c \leq 1.0$.

Source: Adapted from Kays and London (1984).

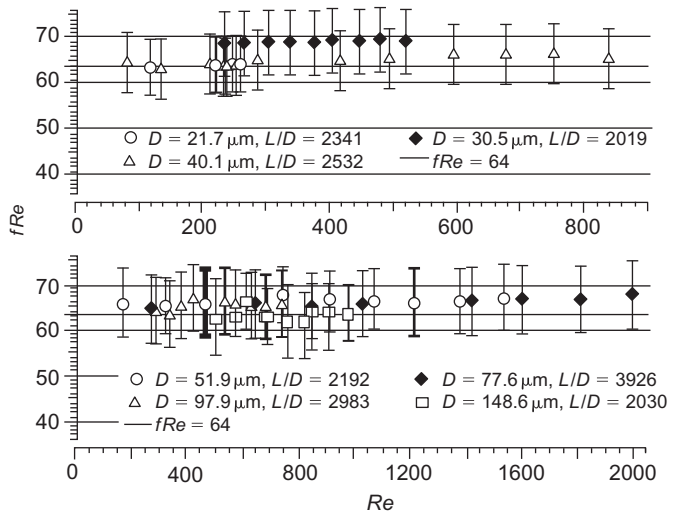
For $L > L_h$, $K(x)$ is replaced by the Hagenbach's factor $K(\infty)$, as discussed in Section 3.2.3. Steinke and Kandlikar (2005a) conducted experiments on square silicon microchannels with $200\text{ }\mu\text{m}$ sides and 10 mm in length, and analyzed the data in detail. A parameter C^* is introduced to represent the ratio of the experimental and theoretical apparent friction factors. Figure 3.6 shows the data before and after applying the corrections in $C^* = f_{app, ex}/f_{app, th}$, where the subscripts ex and th refer to experimental and theoretical values, respectively. The uncorrected data converge to within 30% of the theoretical predictions after all corrections are applied. It is suspected that the high errors are due to slight variations in the channel cross-sectional area over its length, different entrance conditions, and errors associated with interpolations during data reduction.

Figure 3.7 shows the excellent agreement between the laminar flow theory and experimental results obtained by Judy et al. (2002) in $15\text{--}150\text{ }\mu\text{m}$ round and square microchannels made of fused silica and stainless steel with distilled water, methanol, and isopropanol. Similar agreement has been reported by Bucci et al. (2004) with 172 , 290 , and $520\text{ }\mu\text{m}$ diameter stainless steel circular tubes with water in the fully developed laminar flow region.

Niklas and Favre-Marinet (2003) analyzed the flow of water in a network of triangular microchannels with $D_h = 110\text{ }\mu\text{m}$. The contributions due to various

**FIGURE 3.6**

Variation of $C_{app}^* = f_{app,ex}/f_{app,th}$ for a 200- μm square microchannel array after correcting for entrance and exit losses.

**FIGURE 3.7**

Comparison between theory and experimental data of Judy et al. (2002) in 50–150 μm circular and square microchannels in the fully developed laminar region. (Note: f in this figure represents the Darcy friction factor, which is four times the Fanning friction factor used elsewhere in this text.)

losses were carefully analyzed in both their numerical and experimental work. They concluded that the classical theory is applicable to modeling the flow through the entire system.

Another point that needs to be emphasized is the large errors that are associated with microscale experiments, as pointed out by Judy et al. (2002). A detailed analysis was conducted by Steinke and Kandlikar (2005a) for rectangular microchannels using actual measured parameters. Their final expression for uncertainty in estimating the product fRe for rectangular channels is given by:

$$\frac{U_f Re}{fRe} = \left[2\left(\frac{U_p}{\rho}\right)^2 + \left(\frac{U_\mu}{\mu}\right)^2 + \left(\frac{U_{\Delta p}}{\Delta p}\right)^2 + \left(\frac{U_L}{L}\right)^2 + 3\left(\frac{U_Q}{Q}\right)^2 + \left(\frac{U_a}{a}\right)^2 + 5\left(\frac{U_b}{b}\right)^2 + 2\left(\frac{U_a}{a+b}\right)^2 + 2\left(\frac{U_b}{a+b}\right)^2 \right]^{1/2} \quad (3.28)$$

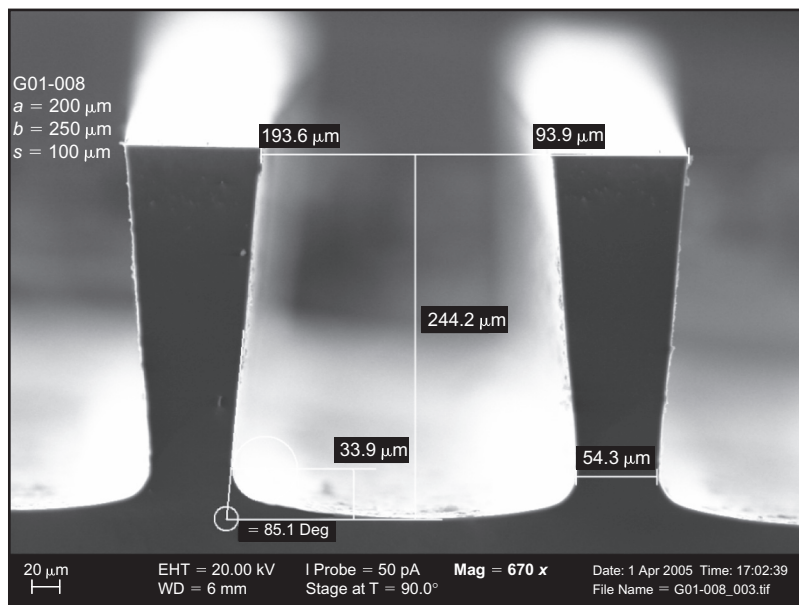
The details of the derivation are given by Steinke (2005). Note that the uncertainties in the measurements of height a and width b have a major influence on the overall uncertainty, followed by the uncertainties in the density and volumetric flow rate measurements. The low-flow Reynolds number data in Figure 3.6 exhibit extremely large uncertainties due to the errors associated with the flow rate measurement. The large discrepancy reported in the literature by some of the earlier investigators is the result of the uncertainties in channel dimensions and flow rate measurements, entrance and exit losses, and the developing region effects.

Figure 3.8 shows a picture of a microchannel cross-section obtained with a scanning electron microscope by Steinke and Kandlikar (2005a). Note that the actual channel profile deviates significantly from the intended rectangular profile. The side walls are undercut by about $20\text{ }\mu\text{m}$ and the corners are rounded. This illustrates the need to accurately measure the flow area for estimating the pressure drop characteristics of microchannels.

Similar conclusions were reached by other investigators, for example, Li et al. (2000), Celata et al. (2002), Judy et al. (2002), Baviere et al. (2004), and Tu and Hrnjak (2003). The increasing deviations from the theoretical values at higher Reynolds numbers in many data sets reported in the literature is believed to be due to the increased length of the developing region. Baviere and Ayela (2004) measured the local pressures along the flow in a microchannel of height $7.5\text{ }\mu\text{m}$. The range of Reynolds numbers considered was between 0.1 and 15. Their results were found to agree with classical theory. They also identified the errors associated with the channel height measurement as being the largest source of uncertainty.

Baviere et al. (2004, 2006) conducted experiments with bronze-, altuglas-, and silicon-coated microchannels with channel heights between 7.1 and $300\text{ }\mu\text{m}$ and channel widths between 1 and 25 mm . Their results were also in excellent agreement with classical theory.

Other effects that may influence the flow in microchannels are (i) high viscous dissipation causing a change in the fluid viscosity at the wall, and

**FIGURE 3.8**

Cross-sectional view of a rectangular microchannel etched in silicon showing distortion in channel geometry from ideal rectangular profile.

Source: From [Steinke and Kandlikar \(2005a\)](#).

(ii) electrokinetic effects, which are covered in Chapter 4. The effect of viscous dissipation is reviewed by [Shen et al. \(2004\)](#). [Xu et al. \(2000\)](#) modeled this effect and found that the velocity profile was modified due to the viscous dissipation. The resulting friction factors were predicted to be lower due to a reduction in the viscosity at higher liquid temperatures. The viscous effect was studied experimentally by [Judy et al. \(2002\)](#). Their pressure drop data correlated well with the theory when they used the average of the inlet and outlet fluid temperatures from their stainless steel microtubes, which were 15–100 μm in diameter. [Koo and Kleinstreuer \(2004a,b\)](#) concluded that viscous dissipation effects increase rapidly with a decrease in the channel dimensions and hence should be considered along with the imposed heat sources at the channel walls.

[Costaschuk et al. \(2007\)](#) also confirmed that the fully developed friction factors were in agreement with conventional theory in both laminar and turbulent flow regions. [Ghajar et al. \(2010\)](#) reviewed the existing literature and reached the same conclusion. They identified relative roughness as an important parameter responsible for deviations from laminar flow theory.

Figure 3.9 shows a plot of the friction factor versus Reynolds number using the experimental data points reported in the literature, as compiled by [Steinke and Kandlikar \(2005a\)](#). The lines represent the theoretical values for different channel

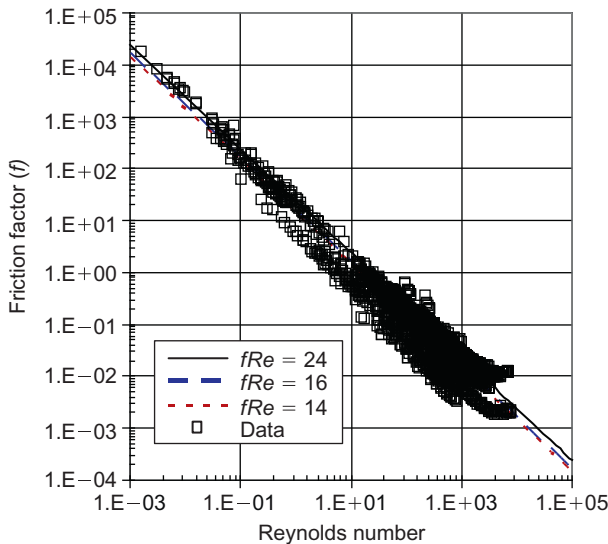


FIGURE 3.9

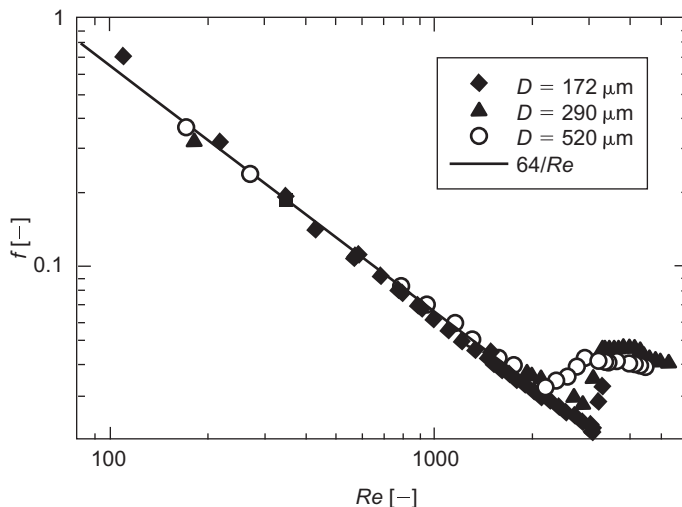
Comparison of friction factors reported in the literature, with the theoretical values for different microchannel geometries. Entrance and exit losses and the developing region at the entrance were not accounted for in a number of data sets reviewed by [Steinke and Kandlikar \(2005a\)](#).

aspect ratios. These data points were screened to eliminate the data that were obtained with large uncertainties and those that did not account for entrance and exit losses. It can be seen that the general trends are followed, though the errors are still quite large, mainly due to the uncertainties associated with channel size measurement.

3.3.2 Laminar-to-turbulent transition

The laminar-to-turbulent flow transition is another topic that has been analyzed by a number of investigators. The laminar-to-turbulent transition in abrupt entrance rectangular ducts was found to occur at a transition Reynolds number of $Re_t = 2200$ for $\alpha_c = 1$ and at $Re_t = 2500$ ([Hartnett et al., 1962](#)) for parallel plates with $\alpha_c = 0$. For other aspect ratios, a linear interpolation between these two values is recommended.

Some of the initial studies indicated an early transition to turbulent flow in microchannels. However, a number of recent studies have shown that the laminar-to-turbulent transition remains unchanged. [Figure 3.10](#), from [Bucci et al. \(2004\)](#), shows that the transition occurred around $Re_t = 2000$ for circular microtubes 171–520 μm in diameter. The results of [Baviere et al. \(2004, 2006\)](#) also indicate that the laminar-to-turbulent transition in smooth microchannels is not influenced by the channel dimensions and occurs around 2300. Similar results were reported by a number of investigators, including [Bucci et al. \(2004\)](#), [Schmitt](#)

**FIGURE 3.10**

Comparison between theory and experimental data of [Bucci et al. \(2004\)](#) in 171–520 μm diameter circular tubes in the fully developed laminar region. (Note: f in this figure represents the Darcy friction factor, which is four times the Fanning friction factor used elsewhere in this text.)

and [Kandlikar \(2005\)](#), and [Kandlikar et al. \(2005\)](#) for minichannels with $D_h < 1 \text{ mm}$, and by [Li et al. \(2000\)](#) for $80 \mu\text{m} \leq D_h \leq 166.3 \mu\text{m}$.

The transition from the laminar-to-turbulent region is influenced by channel surface roughness. Further details of this effect are discussed in the next section.

3.4 Roughness effects

3.4.1 Roughness representation

[Darcy \(1857\)](#) investigated the effects of surface roughness on the turbulent flow of water in rough pipes made of cast iron, lead, wrought iron, and asphalt-covered cast iron. The pipes were 12–500 mm in diameter and 100 m long. [Fanning \(1886\)](#) proposed a correlation for the pressure drop as a function of roughness. [Mises \(1914\)](#) is credited with introducing the term relative roughness, which was originally defined as the ratio of absolute roughness to the pipe radius (we now use pipe diameter to normalize roughness parameters, such as average roughness R_a). [Nikuradse \(1937\)](#) presented a comprehensive review of the literature covering uniform roughness and roughness structures such as corrugations, and some of the available correlations relating friction factor to relative roughness. He also conducted a systematic study on friction factor by applying uniform-diameter sand grain particles with Japanese lacquer to the inner pipe

surface and measuring the pressure drop. He identified three regions which form the basis of the current Moody diagram that is used for friction factor estimation.

The term relative roughness is used for the ratio ε/D_h , where ε is the average roughness. Nikuradse used the diameter of the uniform sand grain particles to represent the roughness ε . The range of relative roughness in Nikuradse's experiments on circular pipes was $0.001 \leq \varepsilon/D \leq 0.033$. Furthermore, Nikuradse identified three ranges to describe his laws of resistances. In Range I, for low Reynolds numbers corresponding to laminar flow, the friction factor was independent of surface roughness and was given by the now-established classical equation $f = 16/Re$ for circular pipes. In Range II, he described the roughness effects on the friction factor in turbulent flow by $f = 0.079/Re^{1/4}$; finally, in Range III, the friction factor is independent of the Reynolds number but depends on the relative roughness, $f = 0.25/[1.74 + 2 \log(2\varepsilon/D)]^2$. Note that the original equations by Nikuradse have been modified to express them in terms of the Fanning friction factor (which is one-fourth of Darcy friction factor, $f = 0.25 f_{\text{Darcy}}$).

[Moody \(1944\)](#) used the available data on the friction factor and developed the well-known Moody diagram covering the relative roughness range of $0 \leq \varepsilon/D \leq 0.05$. Following the earlier investigators, he used the tube root diameter of a circular pipe, similar to Nikuradse's work, in expressing the relative roughness ε/D .

A number of different parameters were studied for their suitability in representing the roughness effects. [Kandlikar et al. \(2005\)](#) investigated parameters based on various roughness characterization schemes and proposed a set of three parameters: mean profile peak height (R_p), mean spacing of profile irregularities (RS_m), and floor distance to mean line (F_p), as shown in [Figure 3.11](#). Two of these parameters (R_p and RS_m) are defined in the [ASME B46.1-2002](#), and the other (F_p) is proposed by [Kandlikar et al. \(2005\)](#).

- *Average maximum profile peak height (R_{pm}):* The distance between the average of the individual highest points of the profile ($R_{p,i}$) and the mean line within the evaluation length. The mean line represents the conventional average roughness value (R_a).

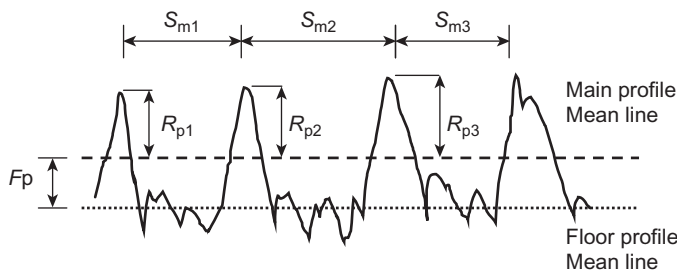


FIGURE 3.11

Maximum profile peak height (R_p), mean spacing of profile irregularities (RS_m), and floor distance to mean line (F_p).

- *Mean spacing of profile irregularities (RS_m):* The mean value of the spacing between profile irregularities within the evaluation length. The irregularities of interest are the peaks, so this is equivalent to the *pitch*.

$$RS_m = \frac{1}{n} \sum_{i=1}^n S_{m_i} \quad (3.29)$$

- *Floor distance to mean line (F_p):* The distance between the main profile mean line (determined by R_a) and the floor profile mean line. The floor profile is the portion of the main profile that lies below the main profile mean line.

The three parameters described above allow the characterization of the peak height, peak spacing, and the distance from the floor to the mean line. These parameters will define the characteristics of the surface roughness that influence the location and shape of the fluid flow streamlines (as described by [Webb et al., 1971](#) and [Kandlikar et al., 2005](#)) and, consequently, the size of the recirculation flow zones between roughness elements. From the above parameters, the equivalent roughness ε can be estimated by the following relationship:

$$\varepsilon = R_{pm} + F_p \quad (3.30)$$

For the sand grain roughness employed by Nikuradse, the new definition of roughness ε yields the same value, and hence no correction is needed for any of the friction factor correlations or charts. The use of mean spacing between profile irregularities is expected to represent the structured roughness surfaces. Such surfaces may be designed in the future to obtain specific pressure drop and heat transfer performance characteristics.

The roughness parameters for a variety of copper, aluminum, stainless steel, nickel, and silicon wafer surfaces produced using different techniques are listed in [Table 3.3](#). The flycut machining was performed with a single-point, carbide-tipped tool bit with a 1-mm radius. The milling was performed with a 12.7-mm-diameter two-flute high-speed steel end mill. The ground samples were prepared using a 60-grit grinding wheel. The silicon wafers were prepared as with KOH etch, XeF_2 etch, and the DRIE process. The nickel comparator surfaces were prepared with milling, grinding, Blanchard grinding, or lapping processes. The values of various roughness parameters used in deriving the roughness parameter εF_p are tabulated. The roughness varies from 0.147 to 6.847 μm . For microchannel passages, these values may be used as roughness values for the specific process used in manufacturing the surface.

3.4.2 Roughness effect on friction factor

Constricted flow model: For microchannels, the relative roughness values are expected to be higher than the limit of 0.05 used in the Moody diagram. [Kandlikar et al. \(2005\)](#) considered the effect of cross-sectional area reduction due to protruding roughness elements and recommended using the constricted flow

Table 3.3 Summary of Roughness Parameters for All Sample Surface
(Parameters in μm)

Roughness Sample	R_a	R_p	R_v	F_p	εF_p
Copper, flycut	0.312	0.817	-0.863	0.225	1.042
Copper, ground	0.290	1.030	-1.818	0.312	1.343
Copper, milled	0.745	0.665	-0.788	0.232	0.896
Aluminum, flycut	0.221	0.792	-0.838	0.228	0.998
Aluminum, ground	0.254	0.849	-1.482	0.269	1.118
Aluminum, milled	0.643	1.908	-1.660	0.213	2.121
Stainless steel, flycut	0.295	0.774	-0.837	0.290	1.065
Stainless steel, ground	0.370	0.999	-1.546	0.328	1.327
Stainless steel, milled	1.195	3.210	-3.098	1.059	4.269
Silicon wafer with KOH etch 0.128	0.337	-0.767	0.149	0.337	
Silicon wafer with XeF_2 etch	-	-	-	-	-
Silicon wafer, DRIE	-	-	-	-	-
Nickel comparator, 2L	0.044	0.118	-0.117	0.028	0.147
Nickel comparator, 4L	0.075	0.182	-0.220	0.056	0.243
Nickel comparator, 8G	0.127	0.449	-0.544	0.174	0.577
Nickel comparator, 8L	0.196	0.548	-0.886	0.218	0.766
Nickel comparator, 16BL	0.452	1.159	-2.410	0.607	1.766
Nickel comparator, 16G	0.389	1.211	-1.441	0.424	1.635
Nickel comparator, 32BL	0.653	1.697	-3.616	0.786	2.484
Nickel comparator, 32G	1.008	2.577	-3.550	1.057	3.634
Nickel comparator, 32ST	0.639	1.770	-2.386	0.649	2.419
Nickel comparator, 63G	1.438	5.293	-8.431	1.555	6.847
Nickel comparator, 63M	1.215	3.668	-4.519	1.380	5.048

area in calculating the friction factor. Using a constricted diameter $D_{cf} = D - 2\varepsilon$, a modified Moody diagram was presented as shown in [Figure 3.12](#). In the turbulent region, it was found that such a representation yielded a constant value of friction factor above $\varepsilon/D_{cf} > 0.03$.

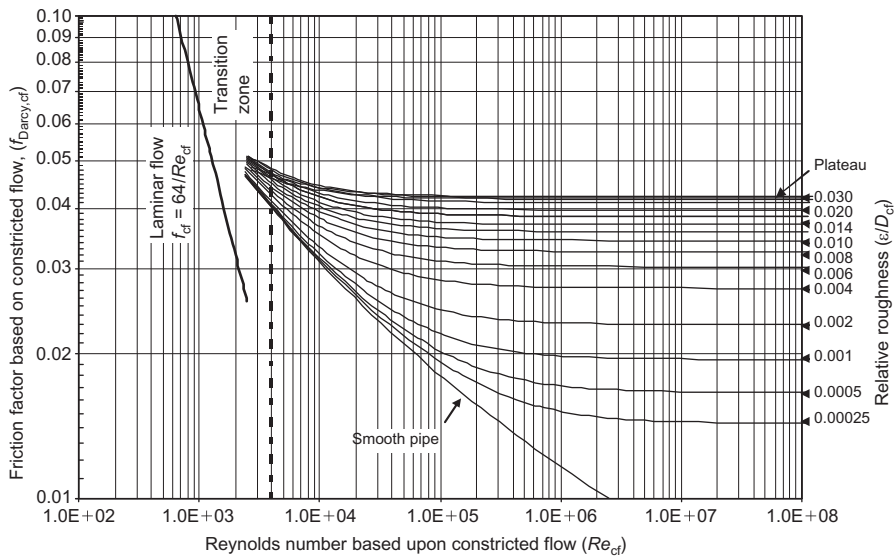
In the turbulent fully rough region, $0.03 < \varepsilon/D_{cf} \leq 0.05$, the friction factor based on the constricted flow diameter is given by:

$$f_{\text{Darcy,cf}} = 0.042 \quad (3.31a)$$

In terms of the Fanning friction factor, we get:

$$f_{cf} = f_{\text{Darcy,cf}}/4 = 0.042/4 = 0.0105 \quad (3.31b)$$

Since experimental data is not available beyond $\varepsilon/D_{cf} > 0.05$, using [Eqs. \(3.31a\)](#) and [\(3.31b\)](#) for higher relative roughness values than 0.05 is not recommended. Note

**FIGURE 3.12**

Darcy friction factor plot based on a constricted flow diameter.

Source: From Kandlikar et al. (2005).

that the friction factor and the geometrical and flow parameters are based on the constricted flow diameter, as given by the following equations:

$$D_{cf} = D - 2\epsilon \quad (3.32)$$

$$\Delta p = \frac{2f_{cf}\rho u_{m,cf}^2 L}{D_{h,cf}} \quad (3.33)$$

$$u_{m,cf} = \dot{m}/A_{cf} \quad (3.34)$$

$$Re_{cf} = \frac{\rho u_{m,cf} D_{h,cf}}{\mu} \quad (3.35)$$

In the fully developed laminar flow region, the constricted friction factor is given by the following equation (Kandlikar et al., 2005):

Laminar region, $0 \leq \epsilon/D_{h,cf} \leq 0.15$

$$f_{cf} = \frac{Po}{Re_{cf}} \quad (3.36)$$

where the Poiseuille number Po is given by either Eq. (3.9) or (3.10) depending on the channel geometry. In the turbulent region, Kandlikar et al. (2005) derived the following expression for f_{cf} using the Colebrook equation.

$$\frac{1}{(D_{cf}+2\varepsilon/D_{cf})^{2.5}f_{Darcy,cf}^{0.5}} = -2.0 \log_{10} \left(\frac{(\varepsilon/D_{cf} + 2\varepsilon)}{3.7} + \frac{2.51}{Re_{cf}(D_{cf}+2\varepsilon/D_{cf})^{1.5}f_{Darcy,cf}^{0.5}} \right) \quad (3.37)$$

Note that the equation given in Kandlikar et al. (2005) contains typographical errors, and the above equation is in the corrected form. However, since it requires an iterative calculation, an alternate form of friction factor suggested by Haaland (1983) is employed to obtain f_{cf} directly without an iterative procedure. In the fully developed turbulent region, $0 \leq \varepsilon/D_{h,cf} < 0.03$, the friction factor is given by

$$f_{cf} = \frac{f_{Darcy,cf}}{4} = \frac{1}{4} \left\{ -18 \log_{10} \left[\left(\frac{1}{3.7(D_{cf}/\varepsilon + 2)} \right)^{1.11} + \frac{6.9}{Re_{cf} \left(\frac{D_{cf}}{D_{cf} + 2\varepsilon} \right)} \right] \right\}^{-2} \left[\frac{1}{1 + \frac{2\varepsilon}{D_{cf}}} \right]^5 \quad (3.38)$$

In the fully developed turbulent region, $0.03 \leq \varepsilon/D_{h,cf} \leq 0.05$ and $Re_{cf} < 10^8$, the friction factor is given by

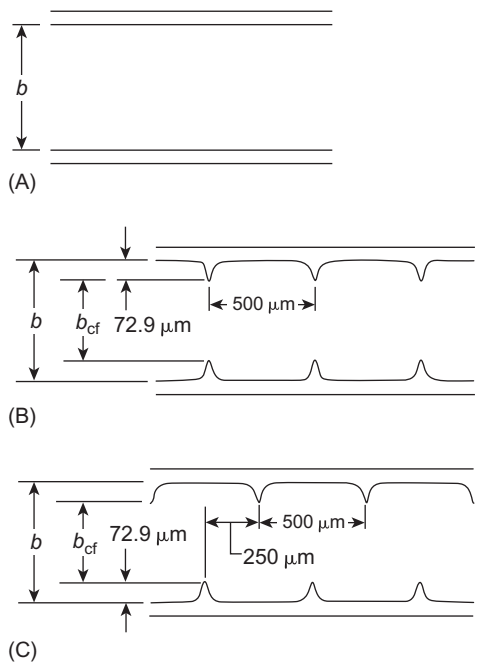
$$f_{cf} = 0.0105 \quad (3.39)$$

Fully developed Darcy friction factors in the turbulent region for roughness ε/D_h , $cf < 0.05$ may be approximated to 0.042 (or Fanning friction factor of 0.0105), as indicated by the modified Moody diagram. Recently, Brackbill and Kandlikar (2010) studied the friction factors for rough channels in the transition and turbulent regions. They found that for structured two-dimensional roughness elements, such as grooves, the fully developed friction factors were reduced as the pitch increased. Eventually the friction factors approached the smooth channel values as the pitch approached infinity. The pitch is thus seen to affect the friction factor to approach the fully developed turbulent value of 0.042 at lower pitches and the smooth channel values at higher pitches. Further experimental work in this area is recommended.

For rectangular channels with all sides having a roughness ε , the mean flow velocity is calculated using the constricted flow area and the constricted channel dimensions of $a_{cf} = a - 2\varepsilon$ and $b_{cf} = b - 2\varepsilon$. The hydraulic diameter is calculated using the constricted channel dimensions.

Schmitt and Kandlikar (2005) conducted experiments to study the effect of a large relative roughness of $\varepsilon/D_{h,cf}$ up to 0.15 in smooth and artificially roughened rectangular minichannels. They introduced sawtooth roughness elements in a 10.3-mm-wide and 100-mm-long test channel. Cross-sectional views of the smooth channels and channels with sawtooth roughness elements are shown in Figure 3.13. The channel gap b_{cf} was varied to produce values of $\varepsilon/D_{h,cf}$ from 0.03 to 0.15. Differential pressure taps for measuring the local pressure drops were located at several locations along the flow length in the fully developed region.

The smooth channel results reported by Kandlikar et al. (2005) closely follow the classical laminar flow theory for friction factor. The experimental data from

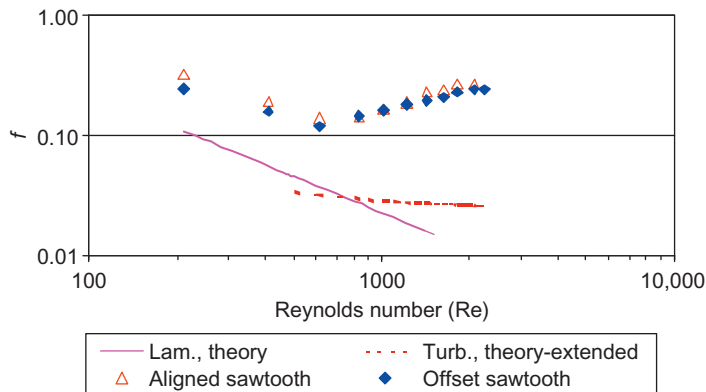
**FIGURE 3.13**

Roughness elements used by Schmitt and Kandlikar (2005) and Kandlikar et al. (2005): (A) smooth channel; (B) aligned sawtooth; and (C) offset sawtooth.

the two sawtooth structures are represented in Figure 3.14 for flow of water with $b = 500 \mu\text{m}$, resulting in a D_h of $953 \mu\text{m}$. This plot uses the height b in calculating D_h and Re . The dashed line represents the $f Re = \text{Constant}$ line corresponding to the channel aspect ratio $\alpha_c = a/b$. It can be seen that the agreement in the low Reynolds number region corresponding to laminar flow is considerably off.

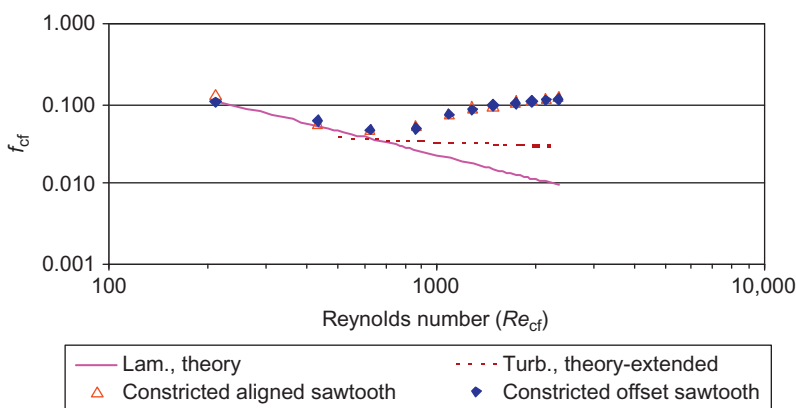
Figure 3.15 shows the same data used in Figure 3.14, but plotted with the constricted flow areas and using the constricted flow parameters given by Eqs. (3.32)–(3.35). The results shown in Figure 3.15 in the laminar region show good agreement with the accepted laminar flow theory ($f_{cf}Re_{cf} = \text{Constant}$).

Similar results were obtained for different gap sizes (yielding different relative roughness values) for both the offset sawtooth and aligned sawtooth geometries. Brackbill and Kandlikar (2010) tested the sawtooth roughness elements of different heights and different pitch to roughness height ratios (β) between 4 and 40, in the relative roughness range from 1.4% to 27.6%. Figure 3.16 shows the results for two roughness elements: (i) a roughness height of $99 \mu\text{m}$ and a pitch of $405 \mu\text{m}$, and (ii) a roughness height of $52 \mu\text{m}$ and a pitch of $1008 \mu\text{m}$. The gap was varied for both cases to yield a range of relative roughnesses shown in Figure 3.16. In the laminar region, although the friction factors were close to the

**FIGURE 3.14**

Fully developed friction factor versus Reynolds number, both based on hydraulic diameter for water flow. $D_h = 953 \mu\text{m}$, $b = 500 \mu\text{m}$, $b_{cf} = 354 \mu\text{m}$, $w = 10.03 \text{ mm}$, $\varepsilon/D_h = 0.0735$.

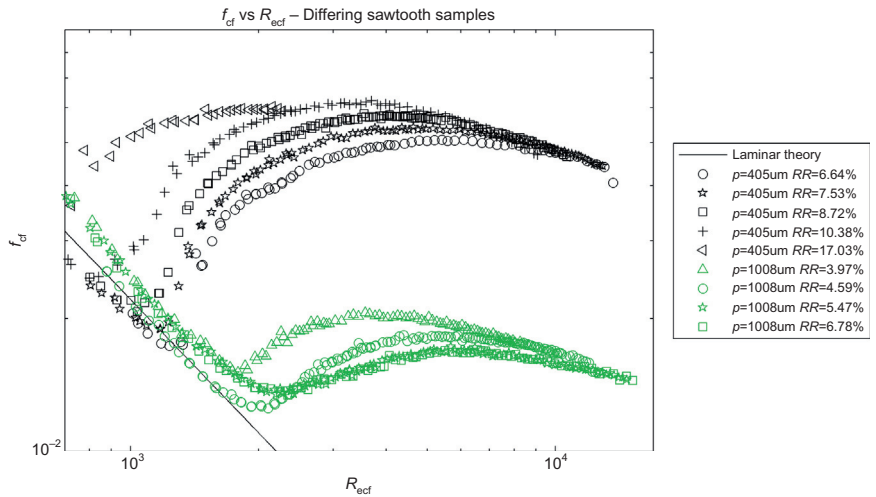
Source: From [Kandlikar et al. \(2005\)](#).

**FIGURE 3.15**

Fully developed friction factor versus Reynolds number, both based on constricted flow hydraulic diameter; water flow. $D_{h,cf} = 684 \mu\text{m}$, $b = 500 \mu\text{m}$, $b_{cf} = 354 \mu\text{m}$, $w = 10.03 \text{ mm}$, $\varepsilon/D_{h,cf} = 0.1108$.

Source: From [Kandlikar et al. \(2005\)](#).

constricted model prediction, a clear effect of pitch was observed. The authors noted that for shorter pitches with pitch to roughness ratios of less than 5, the constricted model is able to predict the friction factor well. For higher pitch to roughness ratios, the friction factor approaches the smooth channel value corresponding to the base of the roughness elements.

**FIGURE 3.16**

Constricted friction factor versus constricted Reynolds number plot with two sawtooth roughness elements and varying channel height in the laminar, transition, and turbulent regions. Upper set of points $\varepsilon_{FP} = 97 \mu m$, $p = 405 \mu m$, lower set of points $\varepsilon_{FP} = 5 \mu m$, $p = 1008 \mu m$.

Wall roughness region-based models: Koo and Kleinsstreuer (2004a,b) considered the roughness region as a porous medium layer at the wall and considered additional viscous forces due to the rough elements present at the wall. The viscous forces were modeled considering the permeability of the porous medium. Baviere et al. (2006) modified the porous layer model by using a discrete element approach to determine the frictional effects of the roughness elements. Subsequently, Gamrat et al. (2008) further extended this model into their rough-layer model (RLM) by considering a periodical distribution of discrete roughness elements on a smooth wall. The total flow resistance is calculated as the sum of the frictional resistance from the bottom of the smooth wall, frictional resistance from the top surface of the roughness elements, and the drag coefficient resulting from the roughness elements. They considered the effect of roughness geometry on the drag coefficient and refined the interface boundary condition between the porous medium and the bulk flow by accounting for the discontinuity at this interface. The analytical model was incorporated into their numerical modeling scheme and compared with the experimental results with a good degree of success for parallelopipedic, circular pin, and random roughness elements.

Lubrication model: Brackbill and Kandlikar (2010) applied lubrication approximation to the rough channels by neglecting the radial velocity component near the roughness elements on the wall and integrating the localized velocity profile. In the laminar region for relative roughness below 5%, the constricted model of Kandlikar et al. (2005) worked very well for lower values of pitch. The results

indicated that the lubrication approximation also worked well for low values of roughness heights, below about 5%. The friction factor approached the smooth channel values as the pitch became larger.

[Wagner and Kandlikar \(2012\)](#) studied sinusoidal roughness elements by considering that the slope of the trajectory of the fluid elements in the vicinity of the roughness elements is small. In other words, the roughness elements provide smoothly varying roughness profiles. The periodic roughness element profiles were fitted with a cosine power function and introduced in the conventional laminar flow equations. The experimental results were compared with the model and it was noted that the effects of geometrical parameters such as pitch and roughness height both can be accounted for with this approach.

3.4.3 Roughness effect on the laminar-to-turbulent flow transition

The transition from laminar-to-turbulent flow has been reported to occur in micro-channels at Reynolds numbers considerably below 2300. In many experiments, the transition has been mistakenly identified to occur early, based on experimental data uncorrected for the developing length ([Steinke and Kandlikar, 2005a](#)). [Kandlikar et al. \(2003\)](#) conducted experiments with stainless steel tubes and noted that early transition occurred for a 0.62 mm ID stainless steel tube with a surface roughness ε/D_h of 0.355%. [Schmitt and Kandlikar \(2005\)](#) conducted careful experiments with plain and sawtooth roughened channels with air and water. Their results for smooth rectangular channels showed a transition Reynolds number between 2000 and 2300, but for increasing relative roughness values there were decreasing transition Reynolds numbers, as seen in [Figures 3.14 and 3.15](#). [Figure 3.17](#) shows the transition Reynolds number as a function of the relative roughness (based on the constricted hydraulic diameter). The following equations are used to describe the roughness effects based on their experimental data.

Laminar-to-turbulent transition criteria:

$$\text{For } 0 < \varepsilon/D_{h,\text{cf}} \leq 0.08: \quad Re_{t,\text{cf}} = 2300 - 18,750(\varepsilon/D_{h,\text{cf}}) \quad (3.40)$$

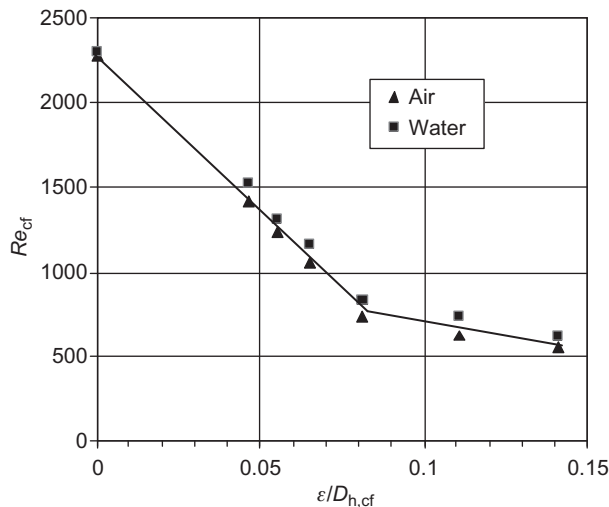
$$\text{For } 0.08 < \varepsilon/D_{h,\text{cf}} \leq 0.15: \quad Re_{t,\text{cf}} = 800 - 3270(\varepsilon/D_{h,\text{cf}} - 0.08) \quad (3.41)$$

[Brackbill and Kandlikar \(2010\)](#) further modified Eq. (3.40) to match the transition Reynolds number for the base channel for a roughness height of zero (smooth channel), Re_0 as follows.

$$\text{For } 0 < \varepsilon/D_{h,\text{cf}} \leq 0.08: \quad Re_{t,\text{cf}} = Re_0 - \frac{(Re_0 - 800)}{0.08}(\varepsilon/D_{h,\text{cf}}) \quad (3.42)$$

The experimental data on the transition Reynolds number by [Brackbill and Kandlikar \(2010\)](#) agrees well with the above model. At a relative roughness value of 27.6%, the turbulent transition was observed to occur at a Reynolds number of only 200.

The friction factor in the transition region for rough tubes with $\varepsilon/D_{h,\text{cf}} < 0.05$ at a given Re_{cf} can be obtained by a linear interpolation of (i) the laminar friction

**FIGURE 3.17**

Transition Reynolds number variation with relative roughness based on constricted flow diameter, Eqs. (3.37) and (3.38) plotted along with data from Schmitt and Kandlikar (2005).

factor obtained from Eq. (3.36) at the transition Reynolds number, and (ii) the turbulent friction factor at $Re_{cf} = 2300$ given by Eq. (3.38) or (3.39) depending on the value of $\varepsilon/D_{h,cf}$. For $\varepsilon/D_{h,cf} > 0.05$ in the transition region, additional experimental data is needed before any recommendations can be made. Brackbill and Kandlikar (2010) present some of the constricted friction factor data in the transition region, as seen in Figure 3.16.

3.4.4 Developing flow in rough tubes

Developing flow in rough tubes has not been explored in the literature. As a preliminary estimate, the methods described in Section 3.2.3 for smooth tubes are recommended, introducing the constricted flow diameter in calculating the flow velocity, Reynolds number, and friction factor. Further research in this area is needed. Figure 3.16 shows the friction factor behavior in the transition region obtained by Brackbill and Kandlikar (2010) for two different roughness element pitches and varying gaps.

3.4.5 Turbulent flow in rough tubes

There are very few studies available on the effect of roughness on the turbulent flow friction factor. For uniform roughness beyond $\varepsilon/D_{cf} > 0.05$ in the fully developed turbulent flow regime, the friction factor based on constricted flow diameter is constant at 0.042, according to the modified Moody diagram given by

Kandlikar et al. (2005). For sawtooth roughness features, Brackbill and Kandlikar (2010) experimentally obtained the friction factors for two different pitches and a range of relative roughnesses. Figure 3.16 shows the values of constricted friction factors versus constricted Reynolds numbers for a rectangular channel with a roughness pitch of 405 and 1008 µm. The relative roughness was varied from 4% to 17%. It is seen that the friction factor in the transition region increases dramatically with a clear effect of relative roughness. However, the curves converge to a single line for each pitch. The asymptotic values decrease as the pitch increases and are below the value of 0.042 for the uniform roughness case.

3.5 Heat transfer in microchannels

3.5.1 Fully developed laminar flow

The Nusselt number in fully developed laminar flow is expected to be constant, as predicted by classical theory. However, there are a number of investigations reported in the literature that show a trend increasing with the Reynolds number in this range. This results from the experimental uncertainties, as discussed in Section 3.5.3.

The Nusselt number in the fully developed laminar flow is constant and depends on the channel geometry and the wall heat transfer boundary condition. Table 3.1 presents the Nusselt numbers for commonly used geometries under axially constant heat flux and circumferentially constant wall temperature (H1) boundary conditions with four-sided heating.

For a rectangular channel, the Nusselt number depends on the channel aspect ratio $\alpha_c = a/b$ and the wall boundary conditions. Three boundary conditions are identified in the literature; the Nusselt number for each one is given below.

Constant wall temperature, T-boundary condition:

$$Nu_T = 7.54(1 - 2.610\alpha_c + 4.970\alpha_c^2 - 5.119\alpha_c^3 + 2.702\alpha_c^4 - 0.548\alpha_c^5) \quad (3.43)$$

Constant circumferential wall temperature, uniform axial heat flux, H1 boundary condition:

$$\begin{aligned} Nu_{H1} = & 8.235(1 - 2.0421\alpha_c + 3.0853\alpha_c^2 - 2.4765\alpha_c^3 \\ & + 1.0578\alpha_c^4 - 0.1861\alpha_c^5) \end{aligned} \quad (3.44)$$

Constant wall heat flux, both circumferentially and axially:

$$\begin{aligned} Nu_{H2} = & 8.235(1 - 10.6044\alpha_c + 61.1755\alpha_c^2 - 155.1803\alpha_c^3 \\ & + 176.9203\alpha_c^4 - 72.9236\alpha_c^5) \end{aligned} \quad (3.45)$$

Dharaiya and Kandlikar (2012) numerically analyzed the rectangular geometry under the axially and circumferentially uniform heat flux (H2) boundary condition. The five conditions studied included heating from (i) all four walls, (ii) only three walls, (iii) only two opposite walls, (iv) only one wall, and (v) only two adjacent walls. Their results for the fully developed laminar flow under these boundary

conditions are shown in [Figure 3.18](#) and are also presented in [Table 3.4](#). They also presented the following correlations based on their numerical results for the fully developed laminar flow Nusselt numbers for these five conditions.

For four walls heated under H2 boundary condition ($0.1 \leq \alpha \leq 1$), case 1:

$$Nu_{H2,f,d,4 \text{ walls}} = [(0.3816)\alpha + 2.886] \quad (3.46)$$

Note that the aspect ratio is defined as the ratio of the smaller to larger side and is always between 0 and 1 for the four walls heated case.

For three walls heated under H2 boundary conditions ($0.1 \leq \alpha \leq 10$), case 2:

$$\begin{aligned} Nu_{H2,f,d,3 \text{ walls}} = & [(1.861 \times 10^{-3})\alpha^6 - (4.864 \times 10^{-2})\alpha^5 + (0.4477)\alpha^4 \\ & - (1.708)\alpha^3 + (2.403)\alpha^2 - (0.4319)\alpha + (2.464)] \end{aligned} \quad (3.47)$$

For two opposite walls heated under H2 boundary conditions ($0.1 \leq \alpha \leq 10$), case 3:

$$\begin{aligned} Nu_{H2,f,d,2 \text{ walls}} = & [(8.464 \times 10^{-3})\alpha^4 - (0.1689)\alpha^3 \\ & + (1.145)\alpha^2 - (3.627)\alpha + (7.121)] \end{aligned} \quad (3.48)$$

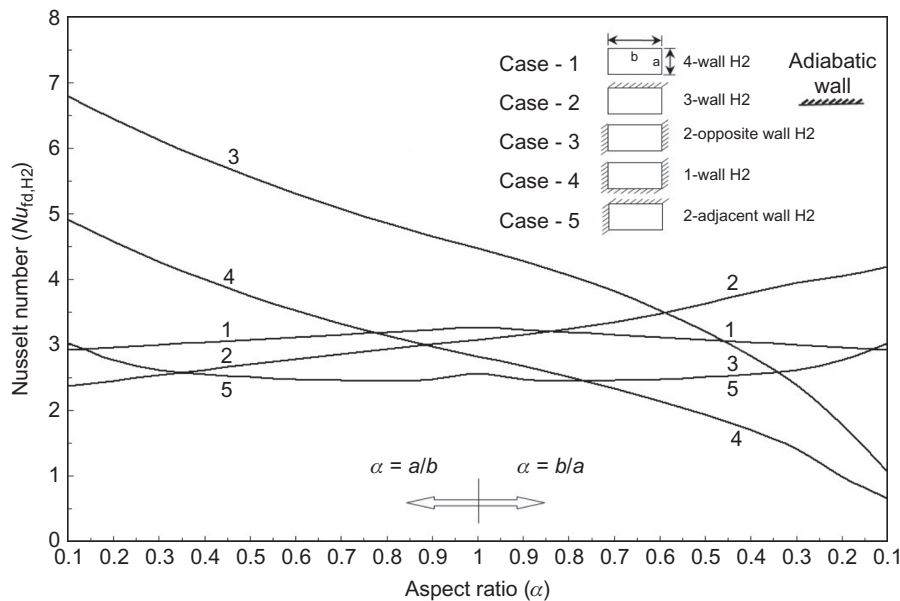


FIGURE 3.18

Nusselt numbers under H2 boundary conditions with heating on (1) all four walls, (2) three walls, (3) two opposing walls, (4) one wall, and (5) two adjacent walls. See [Table 3.5](#) for further details on the wall configuration.

Source: Adapted from [Dharaiya and Kandlikar \(2012\)](#).

Table 3.4 Rectangular Ducts: $Nu_{H2,fd}$ for Fully Developed Laminar Flow, for One or More Walls Heated Under Uniform Heat Flux, H2 Boundary Conditions

Aspect Ratio, $\alpha (a/b)$	Fully Developed Laminar Flow Nusselt Number, $Nu_{H2,fd}$				
	Four-Wall BC	Three-Wall BC	Two-Opposite Wall BC	One-Wall BC	Two-Adjacent Wall BC
0.10	2.924	2.463	6.803	5.036	3.031
0.25	2.981	2.421	6.215	4.358	2.688
0.33	3.029	2.538	6.094	4.151	2.580
0.50	3.115	2.727	5.638	3.744	2.524
0.60	3.113	2.764	5.243	3.456	2.464
0.75	3.110	2.839	4.856	3.172	2.451
1	3.301	3.149	4.614	2.884	2.565
2	3.115	3.277	3.212	1.928	2.524
5	2.962	3.804	1.786	1.019	2.643
10	2.924	4.625	1.067	0.641	3.031

Source: Adapted from [Dharaiya and Kandlikar \(2012\)](#).

For one wall heated under H2 boundary conditions ($0.1 \leq \alpha \leq 10$), case 4:

$$\begin{aligned} Nu_{H2,f,d,2 \text{ walls}} = & [(1.365 \times 10^{-2})\alpha^4 - (0.2563)\alpha^3 \\ & + (1.534)\alpha^2 - (3.825)\alpha + (5.301)] \end{aligned} \quad (3.49)$$

For two adjacent walls heated under H2 boundary conditions ($0.1 \leq \alpha \leq 1$), case 5:

$$\begin{aligned} Nu_{H2,f,d,2 \text{ adjwalls}} = & [(6.1571)\alpha^4 - (14.7340)\alpha^3 \\ & + (13.4030)\alpha^2 - (5.7474)\alpha + 3.4864] \end{aligned} \quad (3.50)$$

Note that for the two adjacent wall heated case, the aspect ratio is defined as the ratio of the smaller to the larger side and is always between 0 and 1.

Cases 1 and 5 represent symmetric wall conditions, and the channel aspect ratio α varies between 0.1 and 1, while cases 2–4 are asymmetric and α varies between 0.1 and 10, as defined in [Table 3.4](#).

In reality, all practical situations fall somewhere in the middle of these three boundary conditions. This becomes an especially important issue in the case of microchannels because of the difficulty in identifying a correct boundary condition with discretely spaced heat sources, and two-dimensional effects in the base and the fins.

The heating in microchannel geometries generally comes from three sides, as a cover of glass or some other material is bonded on top of the microchannels to form the flow passages. The fully developed Nusselt numbers for both three- and four-side heated ducts have been compiled from various sources, including [Wibulswas \(1966\)](#) and [Phillips \(1987\)](#), and are given in [Table 3.5](#). Note that the side with dimension a is not heated, and the channel aspect ratio is defined as $\alpha_c = a/b$.

3.5.2 Thermally developing flow

The thermal entry length is expressed by the following form for flow in ducts:

$$\frac{L_t}{D_h} = c Re Pr \quad (3.51)$$

For circular channels, the leading constant c in [Eq. \(3.51\)](#) is found to be 0.05, while for rectangular channels, the plots presented by [Phillips \(1987\)](#) suggest $c = 0.1$.

The local heat transfer in the developing region of a circular tube is given by the following equations ([Shah and London, 1978](#)):

$$Nu_x = 4.363 + 8.68(10^3 x^*)^{-0.506} e^{-41x^*} \quad (3.52)$$

$$x^* = \frac{x/D_h}{Re Pr} \quad (3.53)$$

Table 3.5 Fully Developed Laminar Flow Nusselt Numbers Under H1 Boundary Conditions

$\alpha_c = a/b$	$Nu_{fd,3}$	$Nu_{fd,4}$
0	8.235	8.235
0.10	6.939	6.700
0.20	6.072	5.704
0.30	5.393	4.969
0.40	4.885	4.457
0.50	4.505	4.111
0.70	3.991	3.740
1.00	3.556	3.599
1.43	3.195	3.740
2.00	3.146	4.111
2.50	3.169	4.457
3.33	3.306	4.969
5.00	3.636	5.704
10.00	4.252	6.700
> 10.00	5.385	8.235

a—unheated side in three-side heated case.

For intermediate values, use the curve-fit equations provided in [Appendix A](#) at the end of the chapter.

For rectangular channels with the four-side heating configuration, Nusselt numbers in the thermally developing region presented in [Table 3.6](#) are derived from [Phillips' \(1987\)](#) work. For the three-side heating configuration, the following scheme is suggested by [Phillips \(1990\)](#).

Three-side heating, $\alpha_c \geq 0.1$ and $\alpha_c \leq 10$, use four-side heating table without any modification.

Three-side heating, $0.1 \leq \alpha_c \leq 10$:

$$Nu_{x,3}(x^*, \alpha_c) = Nu_{x,4}(x^*, \alpha_c) \frac{Nu_{fd,3}(x^* = x_{fd}^*, \alpha_c)}{Nu_{fd,4}(x^* = x_{fd}^*, \alpha_c)} \quad (3.54)$$

The subscripts $x,3$ and $x,4$ refer to the location at a distance x in the heated length for the three-sided and four-sided heating cases, respectively. The Nusselt numbers in the fully developed region for both heating configurations are obtained from [Table 3.5](#); in the developing region Nusselt numbers for the four-sided heating are obtained from [Table 3.6](#).

The use of fully developed hydrodynamic conditions in heat transfer analysis is reasonable for water. [Garimella and Singhal \(2004\)](#) noted that assuming fully developed hydrodynamic conditions and thermally developing conditions resulted in a satisfactory agreement with their data for microchannels.

Table 3.6 Thermal Entry Region Nusselt Numbers

x^*	$\alpha_c \leq 0.1^a$	$Nu_{x,4}$				
		$\alpha_c = 0.25$	$\alpha_c = 0.333$	$\alpha_c = 0.5$	$\alpha_c = 1.0$	$\alpha_c \geq 10^b$
0.0001	31.4	26.7	27.0	23.7	25.2	31.6
0.0025	11.9	10.4	9.9	9.2	8.9	11.2
0.005	10	8.44	8.02	7.46	7.1	9.0
0.00556	9.8	8.18	7.76	7.23	6.86	8.8
0.00625	9.5	7.92	7.5	6.96	6.6	8.5
0.00714	9.3	7.63	7.22	6.68	6.32	8.2
0.00833	9.1	7.32	6.92	6.37	6.02	7.9
0.01	8.8	7	6.57	6.05	5.69	7.49
0.0125	8.6	6.63	6.21	5.7	5.33	7.2
0.0167	8.5	6.26	5.82	5.28	4.91	6.7
0.025	8.4	5.87	5.39	4.84	4.45	6.2
0.033	8.3	5.77	5.17	4.61	4.18	5.9
0.05	8.25	5.62	5.00	4.38	3.91	5.55
0.1	8.24	5.45	4.85	4.22	3.71	5.4
1	8.23	5.35	4.77	4.11	3.6	5.38

$x^* = x/(Re Pr D_h)$
^aParallel plates, both sides heated.
^bParallel plates, one side heated. For intermediate values, use the curve-fit equations provided in Appendix A.

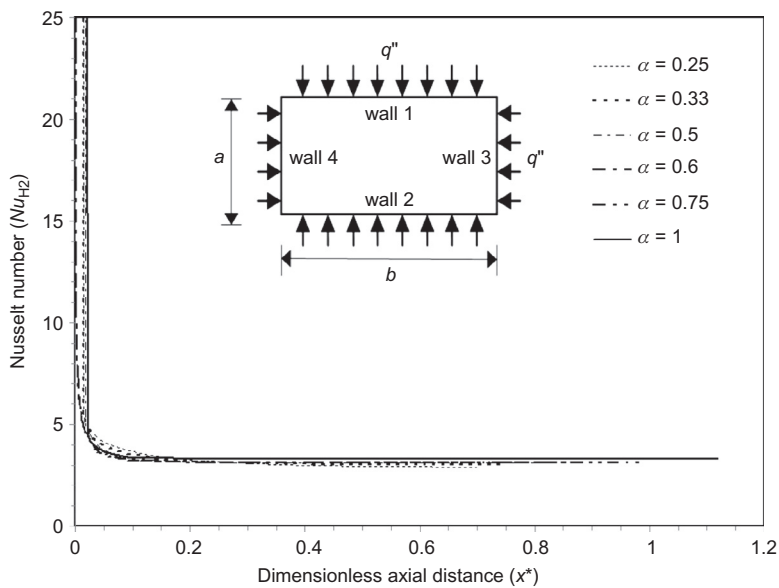
For the H2 boundary conditions, [Dharaia and Kandlikar \(2012\)](#) numerically analyzed the entry region problem. Their results for the five different wall heating configurations are given in [Figures 3.19–3.23](#).

3.5.3 Agreement between theory and available experimental data on laminar flow heat transfer

Laminar flow heat transfer in microchannels has been studied by a number of researchers. Agreement with classical laminar flow theory is expected to hold, but the reported data show significant scatter due to difficulties encountered in making accurate measurements of local heat flux and temperature. [Steinke and Kandlikar \(2005b\)](#) reviewed the available data and presented a comprehensive table showing the range of parameters employed. The laminar flow heat transfer in the fully developed region is expected to be constant, but the data taken from the literature show a generally linear increase in Nusselt number with flow Reynolds number, as seen in [Figure 3.24](#).

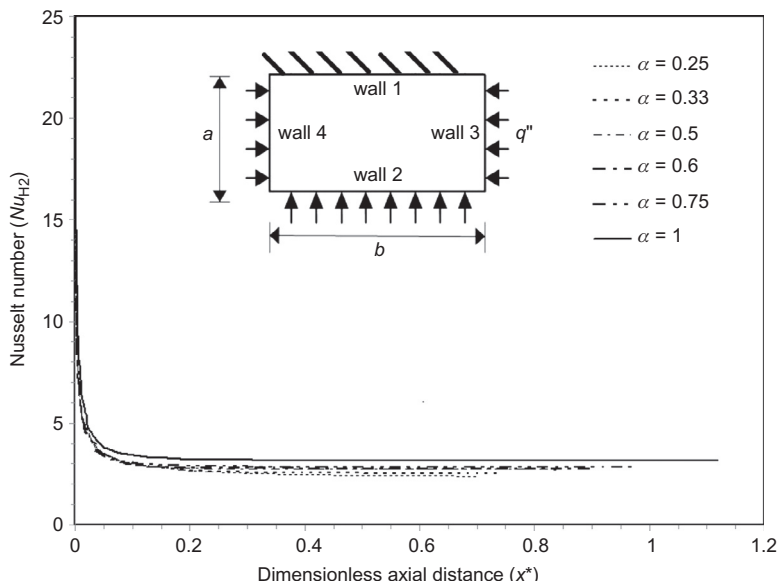
The main reasons for this discrepancy have been attributed to the following factors:

- (i) *Entrance region effects:* The researchers have used the fully developed theoretical values for Nusselt numbers in their comparison with the

**FIGURE 3.19**

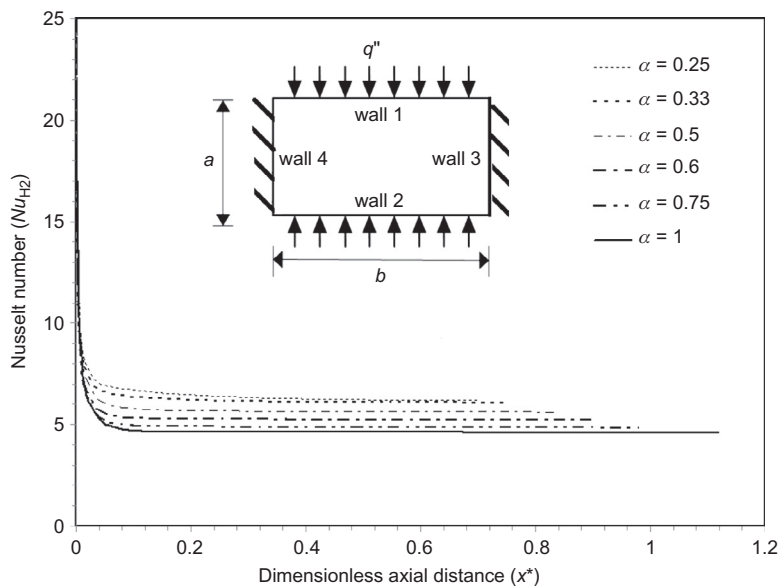
Local Nusselt number as a function of nondimensional length and channel aspect ratio for heating on all four walls, H₂ boundary conditions.

Source: Adapted from [Dharaiya and Kandlikar \(2012\)](#).

**FIGURE 3.20**

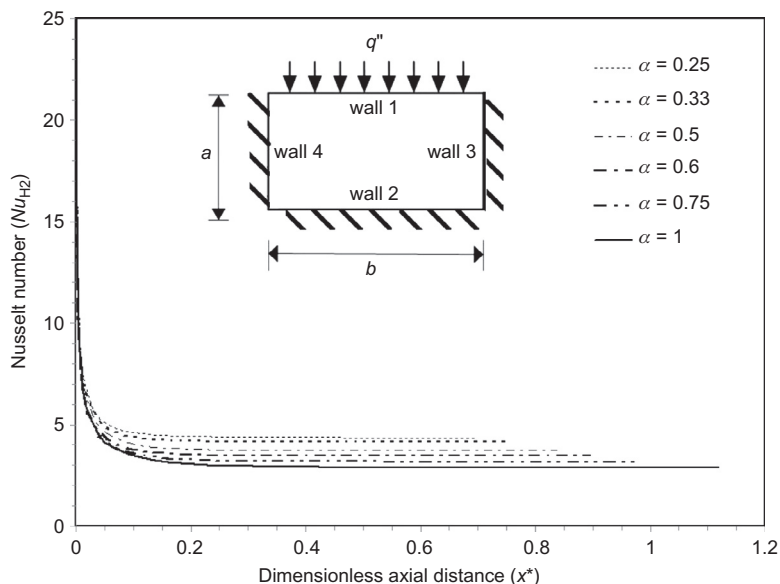
Local Nusselt number as a function of nondimensional length and channel aspect ratio for heating on three walls, H₂ boundary conditions.

Source: Adapted from [Dharaiya and Kandlikar \(2012\)](#).

**FIGURE 3.21**

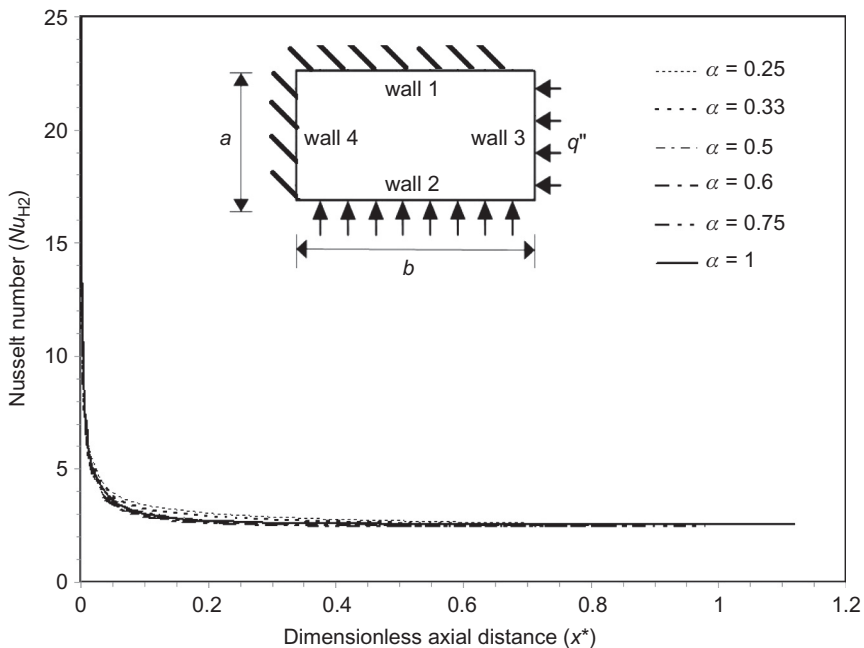
Local Nusselt number as a function of nondimensional length and channel aspect ratio for heating on two opposed walls, H2 boundary conditions.

Source: Adapted from Dharaiya and Kandlikar (2012).

**FIGURE 3.22**

Local Nusselt number as a function of nondimensional length and channel aspect ratio for heating on one wall, H2 boundary conditions.

Source: Adapted from Dharaiya and Kandlikar (2012).

**FIGURE 3.23**

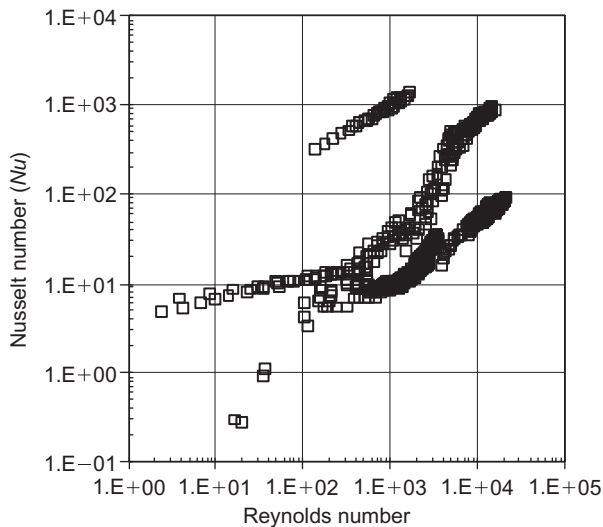
Local Nusselt number as a function of nondimensional length and channel aspect ratio for heating on two adjacent walls, H2 boundary conditions.

Source: Adapted from [Dharaiya and Kandlikar \(2012\)](#).

experimental data. Due to the relatively short lengths employed in microchannels, the influence of the entrance region cannot be neglected. The entrance region effects become more significant at higher Reynolds numbers, in part explaining the trend of increasing Nusselt number with Reynolds number, as seen in [Figure 3.24](#).

- (ii) *Uncertainties in experimental measurements:* The uncertainties in heat transfer measurements have been analyzed by a number of investigators, including [Judy et al. \(2002\)](#) and [Steinke and Kandlikar \(2005b\)](#). The following equation for the uncertainty in Nusselt number calculation from the uncertainties in the experimental measurements is presented by Steinke and Kandlikar for a rectangular channel of base width a and height b :

$$U_{Nu} = Nu \cdot \left[\left(\frac{U_{kf}}{k_f} \right)^2 + \left(\frac{U_L}{L} \right)^2 + \left(\frac{U_V}{V} \right)^2 + 4 \left(\frac{U_{T_s}}{T_s} \right)^2 + 2 \left(\frac{U_{T_i}}{T_i} \right)^2 + 2 \left(\frac{U_{T_o}}{T_o} \right)^2 + 3 \left(\frac{U_a}{a} \right)^2 + 4 \left(\frac{U_b}{b} \right)^2 + 5 \left(\frac{U_{\eta_f}}{\eta_f} \right)^2 \right]^{1/2} \quad (3.55)$$

**FIGURE 3.24**

Selected experimental data for single-phase liquid flow in microchannels and minichannels, $D_h = 50 \mu\text{m}$ to $600 \mu\text{m}$.

where U = uncertainty, I = current, V = voltage, T_s = surface temperature, T_i = fluid inlet temperature, T_o = fluid outlet temperature, L = flow length, a and b = cross-section dimensions, and η_f = fin efficiency. The uncertainties in the measurement of the surface temperature and flow-channel dimensions play a critical role in the overall uncertainty. The importance of accurate geometrical measurement was emphasized in the friction factor estimation as well. Accurate surface temperature measurement poses a significant challenge due to the small dimensions of the test section. Use of silicon chips with integrated circuits to measure the temperatures is recommended.

Another factor that makes the temperature measurements critical in the overall uncertainty estimation is the small temperature difference between the surface and the fluid at the outlet. Since the heat transfer coefficients are very high in microchannels and the flow rate is relatively low (low Reynolds number), the outlet temperature in many experiments approaches the surface temperature. Proper experiments need to be designed to account for this effect.

- (iii) *Ambiguity in the determination of the thermal boundary conditions:* Several experiments reported in the literature were conducted with microchannels or minichannels fabricated on copper or silicon substrates. The actual boundary conditions for these test sections are difficult to ascertain as they fall in between the constant temperature and constant heat flux boundary conditions. Furthermore, in many cases the heating is three-sided, with the side walls acting as fins. The fin efficiency effects also alter the heat flux

and temperature distributions. A clear comparison is only possible after the conjugate heat transfer effects are incorporated into a detailed numerical simulation of the test section.

3.5.4 Heat transfer in the transition and turbulent flow regions

A detailed discussion was presented earlier on the critical Reynolds number for the laminar-to-turbulent transition. For smooth channels, the well-established criterion of $Re_c = 2300$ is expected to hold. The effect of roughness is described by Eqs. (3.42) and (3.41). Since the transition region is encountered in many mini-channel and microchannel heat exchangers, there is a need to generate accurate experimental data for both smooth and rough tubes in this region.

Phillips (1990) suggests using the following equations in the developing turbulent region. For larger values of x , the influence of the term $[1 + (D_h/x)^{2/3}]$ reduces asymptotically to 1:

$$\text{For } 0.5 \leq Pr \leq 1.5: Nu = 0.0214[1.0 + (D_h/x)^{2/3}][Re^{0.8} - 100]Pr^{0.4} \quad (3.56)$$

$$\text{For } 1.5 \leq Pr \leq 1.5: Nu = 0.0214[1.0 + (D_h/x)^{2/3}][Re^{0.8} - 100]Pr^{0.4} \quad (3.57)$$

Further validation of these equations in microchannels is warranted. Adams et al. (1997) conducted experimental work in the turbulent region with flow of water in 0.76- and 0.109-mm diameter circular channels. Based on their data, they proposed the following equation, which matches the data by Yu et al. (1995) within $\pm 18.6\%$:

$$Nu = Nu_{Gn}(1 + F) \quad (3.58)$$

where

$$Nu_{Gn} = \frac{(f/8)(Re - 1000)Pr}{1 + 12.7(f/8)^{1/2}(Pr^{2/3} - 1)} \quad (3.59)$$

$$f = (1.82 \log(Re) - 1.64)^{-2} \quad (3.60)$$

$$F = C Re(1 - (D/D_o)^2) \quad (3.61)$$

Nu_{Gn} represents the Nusselt number predicted by Gnielinski's (1976) correlation. The least-squares fit to all the data sets studied by Adams et al. (1997) resulted in $C = 7.6 \times 10^{-5}$ and $D_o = 1.164$ mm.

Heat transfer coefficients in microchannels are very high due to their small hydraulic diameters. The high pressure gradients have led researchers to employ low flow rates. However, with the reduced flow rate, the ability of the fluid stream to carry the heat away for a given temperature rise becomes limited. In order to improve overall cooling performance, the following two options are available.

1. Reduce the flow length of the channels.
2. Increase the liquid flow rate.

As a result, employing multiple streams with short paths in a microchannel heat exchanger is recommended, similar to a split-flow arrangement, providing two streams, as will be discussed in [Section 3.7](#). The reduced flow length will then enable the designer to employ higher flow rates under a given pressure drop limit. This scheme offers several advantages over a single-pass arrangement where the fluid traverses the entire length of the heat exchanger:

1. *The reduced flow length reduces the pressure drop:* the short flow length effectively reduces the overall pressure drop.
2. *Larger developing region:* the multiple inlets result in a larger channel area under developing conditions where the heat transfer is higher.
3. *Higher flow velocities:* some of the pressure drop reduction could be used to increase the flow velocity of individual streams. The possibility of employing turbulent flow should also be explored as the heat transfer coefficient is higher in this region.

3.5.5 Axial conduction effects

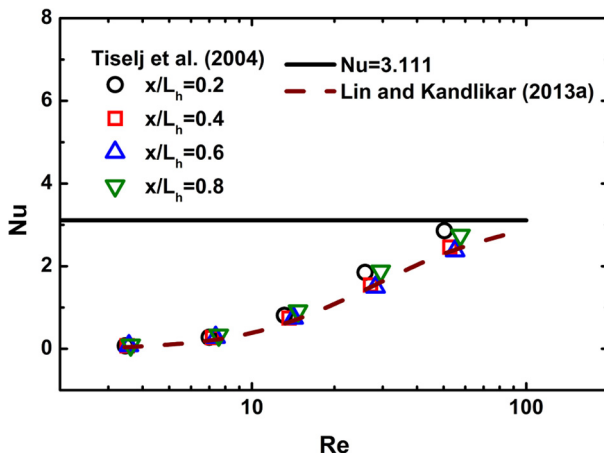
The high heat transfer rates associated with microchannels introduce a temperature gradient along the flow direction in the channel walls. This effect becomes more important at microscale as the channel wall dimensions become comparable to the channel dimensions, and the heat transfer in the walls cannot be neglected. Earlier researchers such as [Guo and Li \(2003\)](#) and [Hetsroni et al. \(2005\)](#) indicated that axial conduction effects may be among the reasons for discrepancies in predicting the heat transfer at microscale.

[Maranzana et al. \(2004\)](#) analyzed heat conduction effects and proposed a parameter M as the ratio of the wall conduction to fluid convection rates. An equation was derived to account for the axial conduction effects in reducing the heat exchanger efficiency. They also derived a set of equations, which were numerically solved to investigate these effects.

[Lin and Kandlikar \(2012a\)](#) considered the axial conduction effects to cause an increased heat transfer to the fluid near the entrance region, leading to a higher heat transfer rate and a higher fluid temperature at any section in the heat exchanger. They derived the following equation to determine the Nusselt number in the presence of axial conduction effects.

$$\frac{Nu_{ko}}{Nu_{th}} = \frac{1}{1 + 4(k_s A_{h,s} Nu_{th} / k_f A_f (RePr)^2)} \quad (3.62)$$

where Nu_{ko} is the Nusselt number neglecting the effect of axial conduction and Nu_{th} is the theoretical Nusselt number accounting for the heat conduction effect. The wall and fluid thermal conductivities are given by k_s and k_f , respectively, and $A_{h,s}$ and A_f are the conduction heat transfer area in the wall and the flow cross-sectional area for fluid flow, respectively. This model was able to predict the heat

**FIGURE 3.25**

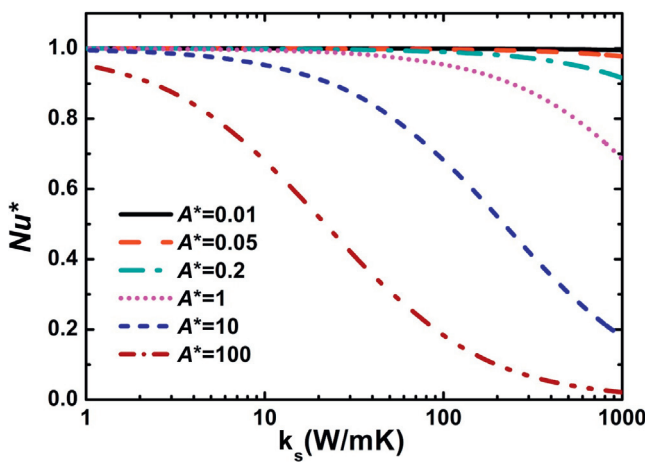
Comparison of the axial conduction model by Lin and Kandlikar (2012a) with the experimental data of Tiselj et al. (2004) for water flow in 160 μm diameter triangular silicon microchannels.

Source: Adapted from Lin and Kandlikar (2012a).

transfer coefficient data available in the literature quite well. Figure 3.25 shows a comparison between the model predictions with the data of Tiselj et al. (2004) for water flow in seventeen 160- μm triangular silicon microchannels for a Reynolds number between 3.2 and 64 for a heated length L_h of 10 mm. The silicon wafer was 530 μm thick and a Pyrex cover of 500 μm thickness was used as a cover plate. The axial conduction area was thus significantly higher than the fluid flow cross-sectional area, and the Reynolds number was quite low. Axial conduction effects are quite severe under these conditions.

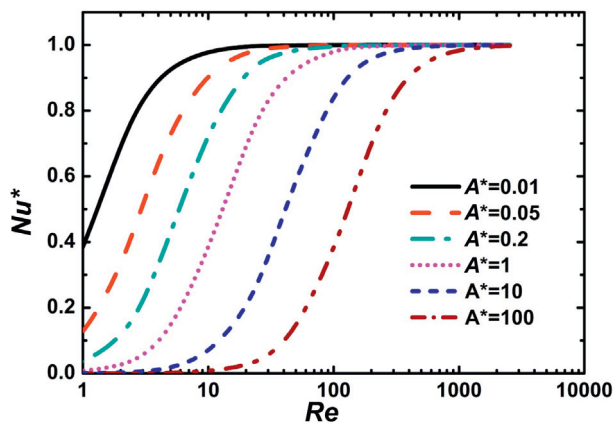
Axial conduction effects become important when the wall cross-sectional area is comparable to the fluid flow area, increasing with an increase in the wall thermal conductivity and a reduction in the fluid Reynolds number. It can be seen from Figure 3.25 that the Nusselt number drops significantly below the theoretical laminar flow value at low Reynolds numbers employed in Tiselj et al.'s experiments. This effect becomes even more significant for gas flow due to the lower thermal conductivity of the fluid.

The effects of wall thermal conductivity on the ratio $Nu^* = Nu_{ko}/Nu_{th}$ are shown in Figure 3.26. The curves are plotted for different area ratios $A^* = A_{h,s}/A_f$ from 0.01 to 100. As the wall thermal conductivity and area ratio increase, the axial conduction effects become quite large and may not be negligible. The effect of cross-sectional area to flow area ratio and Reynolds number on Nu due to axial conduction is similarly shown in Figure 3.27.

**FIGURE 3.26**

Effect of wall thermal conductivity and wall cross-sectional area on Nusselt number due to axial conduction during water flow in microchannels. $Nu^* = Nu_{ko}/Nu_{th}$ and $A^* = A_{h,s}/A_f$.

Source: Adapted from [Lin and Kandlikar \(2012a\)](#).

**FIGURE 3.27**

Effect of Reynolds number and wall cross-sectional area on Nusselt number due to axial conduction during water flow in silicon microchannels. $Nu^* = Nu_{ko}/Nu_{th}$ and $A^* = A_{h,s}/A_f$.

Source: Adapted from [Lin and Kandlikar \(2012a\)](#).

The axial conduction effects are particularly severe for gas flow. [Yang et al. \(2012\)](#) and [Lin and Kandlikar \(2013a,b\)](#) present the results of a detailed investigation on the effects of heat loss, viscous dissipation, and axial conduction on the heat transfer.

3.5.6 Variable property effects

The property ratio method is usually recommended in accounting for property variations due to temperature changes in heat exchanger flow passages. The following equations are recommended for liquids:

$$f/f_{cp} = [\mu_w/\mu_b]^M \quad (3.63)$$

$$Nu/Nu_{cp} = [\mu_w/\mu_b]^N \quad (3.64)$$

where the subscript cp refers to the constant property solution obtained from appropriate equations or correlations. For laminar flow, $M = 0.58$ and $N = -0.14$, and for turbulent flow, $M = 0.25$ and $N = -0.11$ ([Kays and London, 1984](#)).

3.6 Roughness effects on heat transfer in microchannels and minichannels

Recent studies on roughness effects presented in [Section 3.4](#) on friction factor during laminar, transition, and turbulent flows clearly indicate a significant influence of roughness on fluid flow. Similar effects are to be expected in heat transfer.

[Kandlikar et al. \(2003\)](#) studied the heat transfer and pressure drop of laminar flow in smooth and rough stainless steel tubes of 1.067 and 0.62 mm ID. The surface roughness of the inner tube wall was changed by treating it with two different acid mixtures. The surface roughness actually went down after the acid treatment as the protruding peaks in the surface profile were smoothed out. The effect of changes in the relative roughness on pressure drop was minimal, but the heat transfer in the thermal entry region showed a distinct dependence on roughness. [Figure 3.28](#) shows

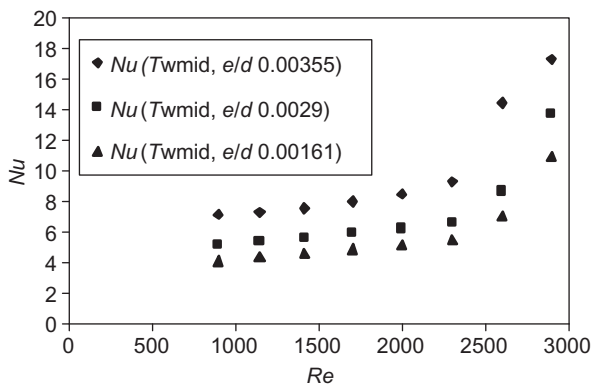


FIGURE 3.28

The effect of roughness on Nu in the thermal entrance region ($x = 52$ mm) of a 0.62 mm inner diameter tube with a fully developed velocity profile and a developing temperature profile ([Kandlikar et al., 2003](#)).

the local Nusselt number at a location 52 mm from the start of the heated length. The flow was hydrodynamically fully developed prior to entering the heated section.

It can be seen from [Figure 3.28](#) that the Nusselt number increases even for a modest increase in the relative roughness from 0.161% to 0.355%. Also note that the location where the heat transfer measurements were taken was preceded by a tube length longer than the hydraulic entry length, which was 380 mm at $Re = 2300$. A number of researchers did not correctly identify the developing region and have mistakenly reported the increasing trend in the Nu versus Re plot as being in the fully developed region.

[Dharaiya and Kandlikar \(2013\)](#) numerically analyzed a two-dimensional sinusoidal roughness profile, shown in [Figure 3.29](#). The width of the channel was 12.7 mm and the flow length was 114.3 mm. The simulations were validated with the laminar flow in smooth minichannels. They also studied the effects of abrupt and smooth entrances on friction factor and heat transfer in the entrance region, and found little difference between the two cases.

The effects of pitch and roughness height were systematically investigated by [Dharaiya and Kandlikar \(2013\)](#). The numerical results for rough channels were compared with the friction factors and Nusselt numbers obtained using the constricted flow diameter in fully developed laminar flow equations. Both friction factor and Nusselt number agreements were fairly good, within 10% for relative roughness values below 5% and pitch to roughness ratios from 2.5 to 25. The results indicated that the pitch to roughness ratio has a strong influence on Nusselt number enhancement. Very high enhancements of over 250% were noted for pitch to roughness ratios of 12.5 and 16; corresponding Nu were 19.3 and 17.2, respectively, for a separation of 550 μm and a pitch of 250 μm . The corresponding friction factor increase was only 30%. [Figure 3.30](#) shows the velocity vectors from their simulation. The velocity vectors indicate that the reason for such high heat transfer enhancement with a relatively low friction factor increase was attributed to the smooth sinusoidal profile. Further details may be obtained

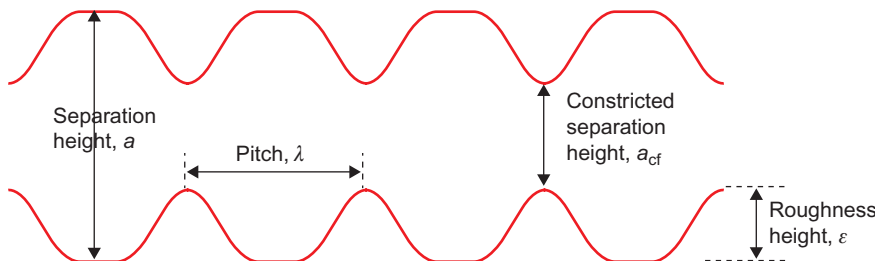


FIGURE 3.29

Two-dimensional roughness geometry analyzed by [Dharaiya and Kandlikar \(2013\)](#) with sinusoidal roughness profile.

Source: Adapted from [Dharaiya and Kandlikar \(2013\)](#).

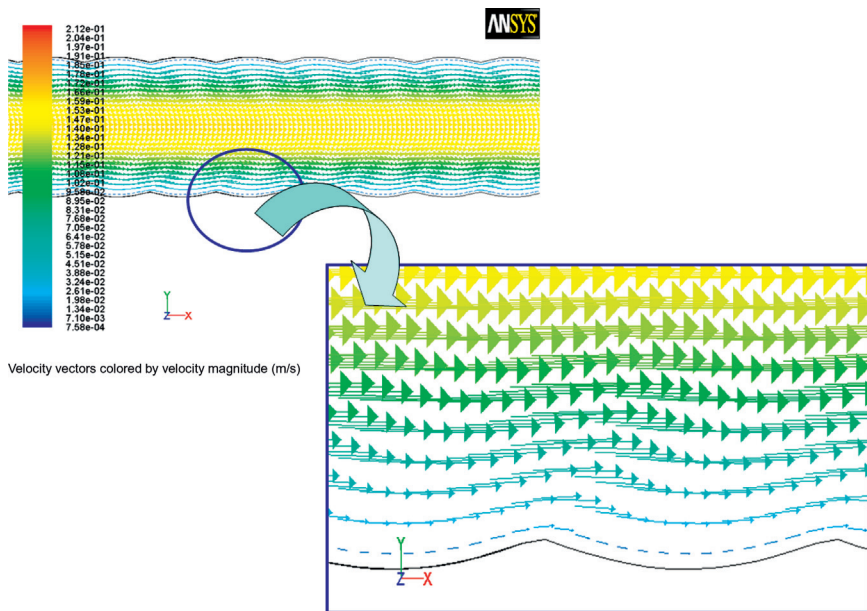


FIGURE 3.30

Velocity vectors for a roughness geometry with channel separation $a = 550 \mu\text{m}$, pitch $\lambda = 250 \mu\text{m}$, and roughness height $\varepsilon = 20 \mu\text{m}$.

Source: Adapted from [Dharaiya and Kandlikar \(2013\)](#).

from [Dharaiya and Kandlikar \(2013\)](#). These model predictions were confirmed experimentally by [Lin and Kandlikar \(2012b\)](#).

[Lin and Kandlikar \(2012b\)](#) conducted a systematic experimental study as a complement to the numerical study by [Dharaiya and Kandlikar \(2013\)](#) discussed above. Eight sets of structured roughness geometries with sinusoidal profile were tested. The opposing walls of a 12.7-mm-wide channel were made of these roughness elements, and the gap was varied to achieve different relative roughness values. The height of the roughness elements varied from 18 to 96 μm , and the roughness pitch varied from 250 to 400 μm . The hydraulic diameter ranged from 0.71 to 1.87 mm, while the constricted diameter ranged from 0.68 to 1.76 mm.

The roughness elements were heated with silicone film heaters attached with adhesive on the back of the roughness elements. The experimental data indicated that the heat losses from the inlet and outlet ends played a significant role in evaluating the heat transfer coefficients. An elaborate scheme was applied to accurately estimate the heat losses in different sections. The heat transfer coefficients were obtained at 11 locations along the flow length after correcting for the heat losses and axial conduction effects. The sinusoidal elements tested provided considerable enhancement, with the maximum enhancement (a factor of 3.77 increase) was provided by a roughness element identified as B-1, with a pitch of

250 μm and a roughness height of 96 μm . The friction factor increase was also quite high, at 3.71. The second best performing roughness element was D-2 (Nu enhancement factor of 1.98, friction factor enhancement factor of only 1.03), with a pitch of 400 μm and a roughness height of 38 μm .

Sinusoidal roughness elements provided the highest heat transfer enhancement for a given friction factor enhancement. The authors defined an enhancement efficiency as

$$\eta = \frac{Nu/Nu_{\text{th,plain}}}{(f/f_{\text{th,plain}})^{1/3}} \quad (3.65)$$

The enhancement efficiency was 2.44 for the roughness element B-1 and 1.96 for the element D-2. These values were compared with some of the most efficient techniques reported in the literature. Figure 3.31 shows a comparison of these techniques. Wongcharee and Eiamsa-ard (2011) used alternate clockwise and counter-clockwise twisted tapes with a heat transfer enhancement factor from 6 to 13, but the friction factor increase was from 8- to 15-fold. The porous medium studied by Huang et al. (2010) had a heat transfer enhancement factor of 5.5 to 4.5; the friction factor increased by a factor of 50–60. Similar observations were made by Krishna et al. (2009) with twisted tapes and by Akhavan-Behabadi et al. (2010) for coiled inserts.

The roughness profile results in an early transition to turbulent region. The enhancement in the turbulent region is also quite high, as seen from Figure 3.31. Roughness geometries with smoothly varying 2d profiles are thus seen as an effective way to enhance heat transfer at microscale.

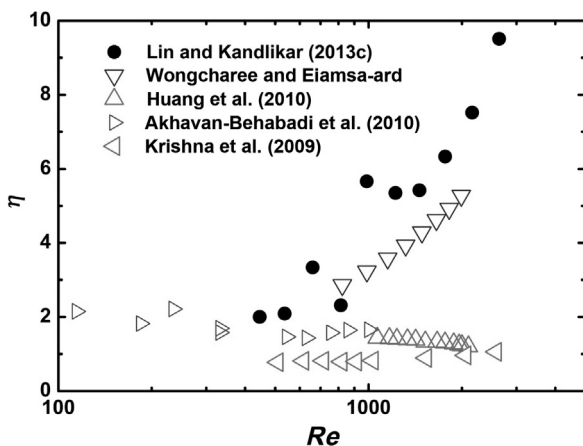


FIGURE 3.31

Comparison of enhancement factor η of B-1 with other available enhancement techniques from recent literature.

Source: Adapted from Lin and Kandlikar (2012b).

3.7 Heat transfer enhancement with nanofluids

Particles with at least one of their dimensions in the nanoscale range are termed nanoparticles. Nanofluids consist of these nanoparticles dispersed in a base liquid phase. Choi (1995) showed that the thermal conductivity of nanofluids is enhanced over the base fluid. The addition of nanoparticles was also reported to alter the specific heat of the mixture by Bergman (2009). This has been a very active topic of research in the last decade, but the effect of nanoparticles on the transport characteristics has not yet been clearly described, and their efficacy in enhancing single-phase heat transfer still remains an open question.

Chein and Huang (2005) performed numerical studies on heat transfer enhancement with Cu nanoparticles in water in various volumetric concentrations. Koo and Kleinstreuer (2005) also presented similar numerical studies. They considered two different microchannels with (i) $100\text{ }\mu\text{m} \times 300\text{ }\mu\text{m}$, and (ii) $57\text{ }\mu\text{m} \times 365\text{ }\mu\text{m}$ channel cross-sectional dimensions. Their results showed that the pressure drop increased only marginally, while the thermal resistance of the heat sink dropped by as much as 50%. A number of researchers have reported analytical and numerical studies showing different levels of enhancement depending on the analytical models used in describing the thermal properties of the nanofluids.

Very few experimental studies on heat transfer with nanofluids have been reported in the literature. Wen and Ding (2004) studied the effect of nanofluids made of $\gamma\text{-Al}_2\text{O}_3$ particles in deionized water in a 4.5-mm-diameter and 970-mm-long copper tube in the laminar region. They found that the heat transfer coefficient enhancement was as much as 47% in the entrance region. This enhancement almost disappeared in the fully developed region. They postulated that the nanoparticles reduced the thermal boundary layer thickness in the entrance region. Nanoparticle migration within the boundary layer was proposed as an enhancement mechanism in nanofluids.

Lee and Mudawar (2007) conducted analytical and experimental studies in laminar and turbulent flow regions with Al_2O_3 nanoparticle suspensions in water. Their theoretical study showed that the friction factor was changed slightly, but the pressure drop increased because of the increased viscosity of the nanofluids. The experiments were performed with the nanofluid at 1% and 2% volume concentrations in deionized water. Thermal conductivity was measured to increase by 6% for the 2% concentration nanofluid. A test setup with 21 parallel channels with 215- μm -wide and 821- μm -deep grooves, with a hydraulic diameter of 341 μm over a 1 cm^2 area was used. The heat transfer enhancement was observed mainly in the entrance region, with only a modest improvement in the fully developed region. The enhancement increased with the concentration of nanoparticles. These observations are in agreement with the experimental results of Wen and Ding (2004) for a larger tube diameter of 4.5 mm.

Recently, Singh et al. (2011, 2012) conducted experimental and numerical investigations to study the hydrodynamics and thermal effects of nanofluids. They used alumina nanofluids in 0.25%, 0.5%, and 1% volume concentrations in three

single microchannels of 130, 211, and 300 μm hydraulic diameter silicon microchannels. The cross-section of the channel was trapezoidal with side angles of 54.74°. The viscosity of the nanofluid reported in the literature was seen to have a significant scatter, varying as much as 50%. The friction factor trends are seen to depend on the channel size, shape, and nanoparticle concentration. An early transition was noticed with nanofluids, but the effect of channel roughness also seemed to play a role. The trends observed are quite different, and it is not clear whether the heat losses and the end effects were adequately considered in the single microchannel test section. The results by [Jung et al. \(2009\)](#) on single microchannel sections indicates a Nusselt number as low as 0.1, and validation with single-phase experiments with pure water is seen as essential before evaluating nanofluid trends.

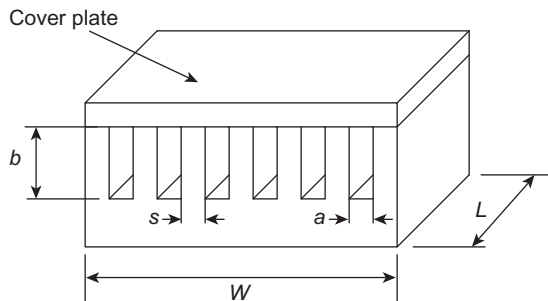
3.8 Microchannel and minichannel geometry optimization

The first practical implementation of microchannels in silicon devices was demonstrated by [Tuckerman and Pease \(1981\)](#). They were able to dissipate 7.9 MW/m² with a maximum substrate temperature rise of 71°C and a pressure drop of 186 kPa. The allowable temperature differences and the pressure drops for cooling today's microprocessor chips have become significantly smaller, and many investigators have been working toward optimization of the channel geometrical configuration.

The application of microchannels to electronics cooling imposes severe design constraints on the system design. For a given heat dissipation rate, the flow rate, pressure drop, fluid temperature rise, and fluid inlet to surface temperature difference requirements necessitate optimization of the channel geometry. A number of investigators have studied the geometrical optimization of microchannel heat exchangers, including [Phillips \(1987\)](#), [Harpole and Eninger \(1991\)](#), [Knight et al. \(1992\)](#), [Ryu et al. \(2002\)](#), [Bergles et al. \(2003\)](#), and [Kandlikar and Upadhye \(2005\)](#). The results found by Kandlikar and Upadhye are presented below.

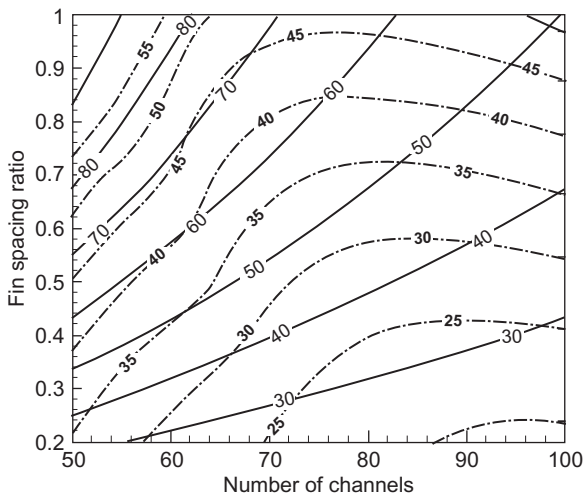
[Kandlikar and Upadhye \(2005\)](#) considered a microchannel system as shown in [Figure 3.32](#). For a chip of width $W = 10 \text{ mm}$ and length $L = 10 \text{ mm}$, they presented an analysis scheme for heat transfer and pressure drop by incorporating the entrance region effects. The number of channels was used as a parameter in developing the optimization scheme. The maximum chip temperature was set at 360 K while the fluid inlet temperature was set equal to 300 K. The channel depth was assumed to be 200 μm .

[Figures 3.33 and 3.34](#) show the parametric plots resulting from the optimization program. The fin spacing ratio, defined as $\beta = s/a$, is plotted as a function of the number of channels on a 10-mm-wide chip with pressure drop, water flow rate, and fin thickness as parameters. A lower limiting value of approximately 40 μm was considered achievable for fin thickness using silicon microfabrication techniques. For a given pressure drop limit, the optimal number of channels and other channel geometrical parameters can be determined from this plot. Such plots could be generated for other system configurations as well.

**FIGURE 3.32**

Microchannel geometry used in microprocessor heat sink channel size optimization.

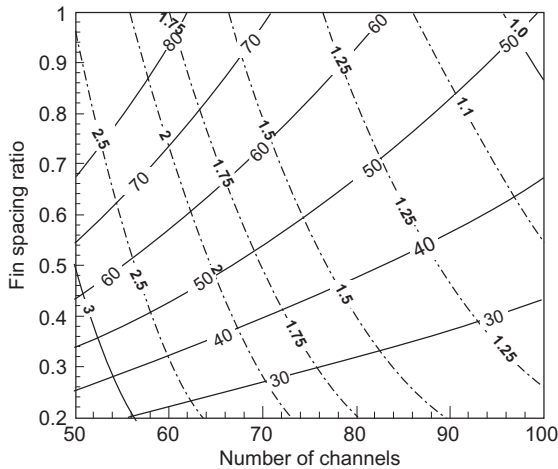
Source: From *Kandlikar and Upadhye (2005)*.

**FIGURE 3.33**

Contour plot of fin spacing ratio β versus the number of channels with pressure drop across them in kilopascal (dash-dot lines) and fin thickness in microns (solid lines) as parameters for water flow in plain rectangular microchannels in a single-pass arrangement at a heat flux of 3 MW/m^2 .

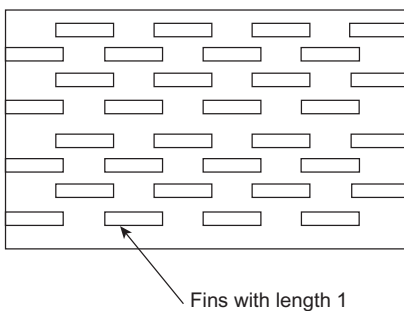
Source: From *Kandlikar and Upadhye (2005)*.

The effect of introducing offset strip-fins in the microchannel flow passages and a split-flow arrangement, as shown in Figures 3.35 and 3.36, respectively, was also analyzed by *Kandlikar and Upadhye (2005)*. The resulting pressure drop versus the dissipated heat flux is shown in Figure 3.37. It can be seen that the pressure drop is reduced considerably in the split-flow arrangement.

**FIGURE 3.34**

Contour plot of fin spacing ratio β versus the number of channels with water flow rate in 10^{-3} kg/s (dash-dot lines) and fin thickness in microns (solid lines) as parameters for water flow in plain rectangular microchannels in a single-pass arrangement at a heat flux of 3 MW/m^2 .

Source: From [Kandlikar and Upadhye \(2005\)](#).

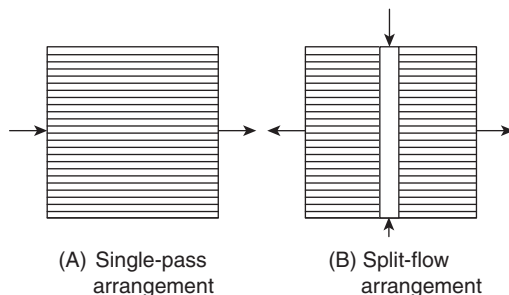
**FIGURE 3.35**

Offset strip-fins shown in the top view, with individual fin length l along the flow length.

Source: From [Kandlikar and Upadhye \(2005\)](#).

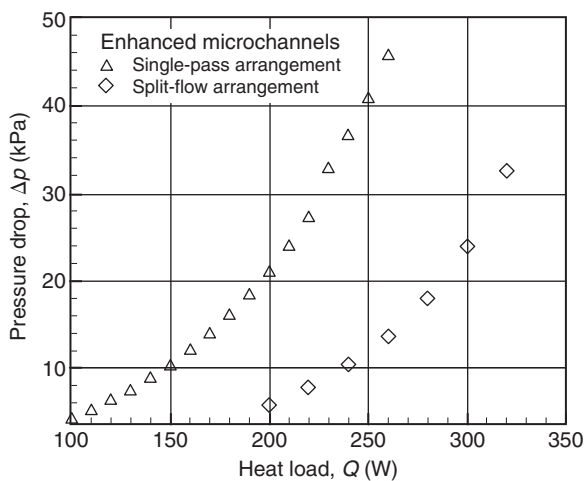
3.9 Enhanced microchannels

The use of enhanced microchannels was proposed by [Kishimoto and Sasaki \(1987\)](#). The need for higher heat transfer coefficients than those attainable with plain microchannels was identified by [Kandlikar and Grande \(2004\)](#), and some specific enhancement geometries were suggested by [Steinke and Kandlikar \(2004a,b\)](#). [Kandlikar and Upadhye \(2005\)](#) analyzed the enhanced-offset strip-fin geometry; the results were presented in the previous section.

**FIGURE 3.36**

Schematics of single-pass and split-flow arrangements for fluid flow through microchannels: (A) single-pass arrangement and (B) split-flow arrangement.

Source: From [Kandlikar and Upadhye \(2005\)](#).

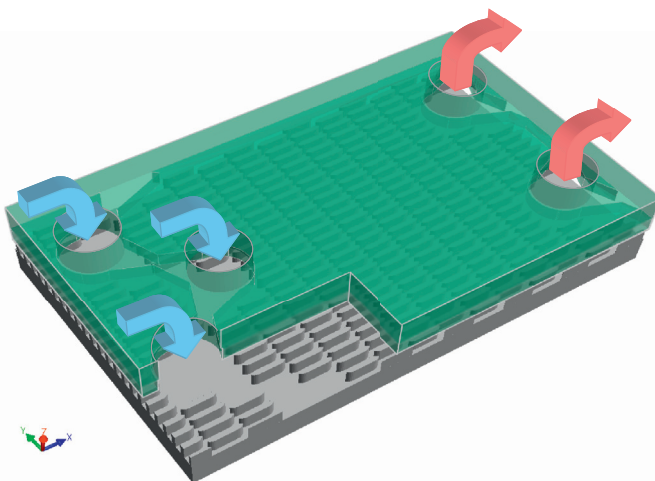
**FIGURE 3.37**

Comparison of pressure drops for the enhanced microchannels with offset strip-fins ($l = 0.5$ mm) in single-pass and split-flow arrangements on a $10\text{ mm} \times 10\text{ mm}$ chip.

Source: From [Kandlikar and Upadhye \(2005\)](#).

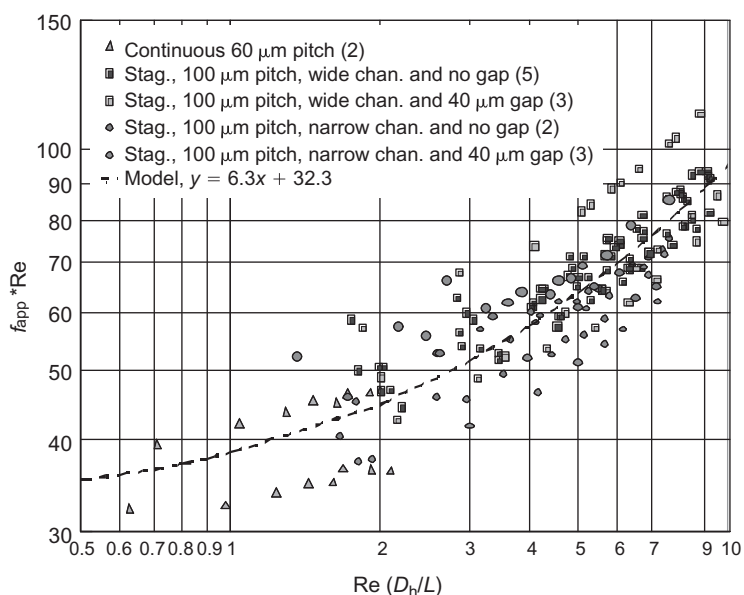
[Colgan et al. \(2005\)](#) presented detailed experimental results comparing various offset fin geometries. A three-dimensional rendition is shown in [Figure 3.38](#). There are several inlet and outlet manifolds, with short flow lengths through the enhanced structures.

The apparent friction factors and Nusselt numbers for plain and several enhanced configurations are shown in [Figures 3.39](#) and [3.40](#). A plot of f_{app} versus Stanton number is shown in [Figure 3.41](#). The relationship deviates somewhat from a linear behavior because the manifold effects are included in the data.

**FIGURE 3.38**

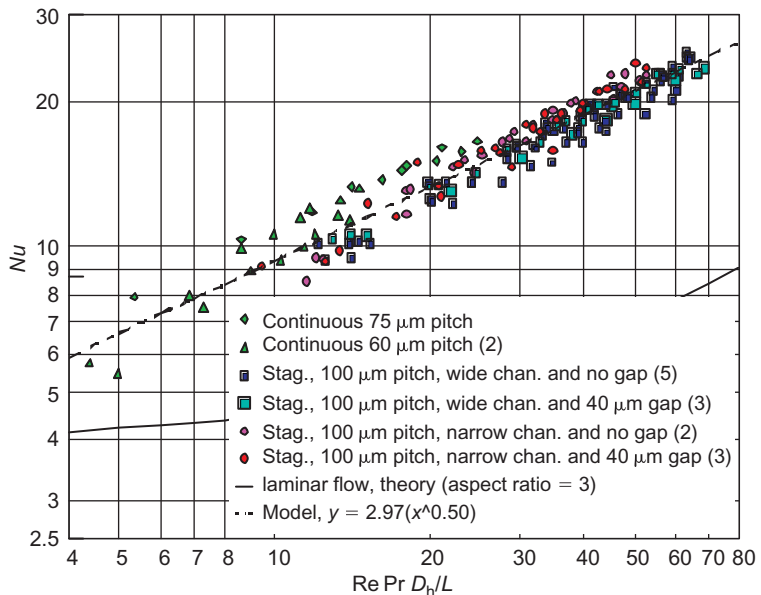
Three-dimensional rendition of the IBM enhanced silicon chip with short multiple fluid streams.

Source: From Colgan et al. (2005).

**FIGURE 3.39**

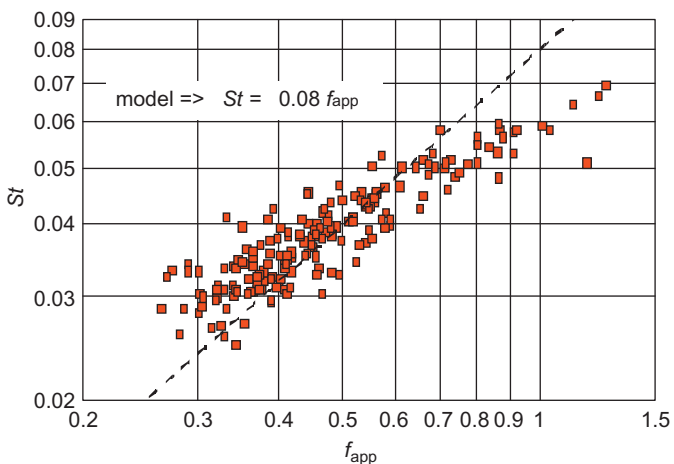
Apparent friction factor comparison of one plain and five enhanced microchannel configurations.

Source: From Colgan et al. (2005).

**FIGURE 3.40**

Nusselt number comparison of one plain and five enhanced microchannel configurations.

Source: From [Colgan et al. \(2005\)](#).

**FIGURE 3.41**

Stanton number and friction coefficient relationship for microchannels with different fin geometries.

Source: From [Colgan et al. \(2005\)](#).

Microfabrication technology opens up a whole new set of possibilities for incorporating enhancement structures derived from past experience in compact heat exchanger development. Different manufacturing constraints enter into play for microchannels on a copper substrate as compared to the silicon microfabrication technology. Novel developments are expected to arise as we continue forward in integrating the microfabrication technology using creative ways to achieve high-performance heat transfer devices. [Steinke and Kandlikar \(2004a,b\)](#) presented a good overview of single-phase enhancement techniques and illustrate various enhancement configurations that may be considered, especially with silicon microfabrication technology.

3.10 Solved examples

Example 3.1

Microchannels are directly etched into silicon in order to dissipate 100 W from a computer chip over an active surface area of 10 mm × 10 mm. The geometry may be assumed similar to [Figure 3.32](#). Each of the parallel microchannels has a width $a = 50 \mu\text{m}$, depth $b = 350 \mu\text{m}$, and a spacing $s = 40 \mu\text{m}$. The silicon thermal conductivity may be assumed to be $k = 180 \text{ W/m K}$.

Assume a uniform heat load over the chip base surface and a water inlet temperature of 35°C. Assume one-dimensional steady state conduction in the chip substrate.

- i. Calculate the number of flow channels available for cooling.
- ii. Assuming the temperature rise of the water to be limited to 10°C, calculate the required mass flow rate of the water.
- iii. Calculate the flow Reynolds number using the mean water temperature for fluid properties.
- iv. Check whether the fully developed flow assumption is valid.
- v. Calculate the average heat transfer coefficient in the channels.
- vi. Calculate fin efficiency.
- vii. Assuming the heat transfer coefficient to be uniform over the microchannel surface, calculate the surface temperature at the base of the fin at the fluid inlet and fluid outlet sections.
- viii. Calculate the pressure drop in the core of the microchannel.
- ix. If two large reservoirs are used as the inlet and outlet manifolds, calculate the total pressure drop between the inlet and the outlet manifolds.

Solution

Properties: Water at 40°C

$$\rho = 991.8 \text{ kg/m}^3; \mu = 655 \times 10^{-6} \text{ N s/m}^2; c_p = 4179 \text{ J/kg K}; k = 0.632 \text{ W/m K}; \\ Pr = 4.33$$

(i) Number of flow channels (Answer: 111 channels).***Assumptions***

- (1) The first and the last channels are half the channel width from the chip edge.

The remaining width left for channels is: $10 \text{ mm} - 50 \mu\text{m} = 0.00995 \text{ m}$.

The pitch is: $50 \mu\text{m} + 40 \mu\text{m} = 90 \mu\text{m} = 90 \times 10^{-6} \text{ m}$.

Assumption 1 requires that the pitch repeat up to the last channel, but not include the last channel.

Therefore, the number of channels is found by $(0.00995 \text{ m} - 50 \times 10^{-6} \text{ m}) / (90 \times 10^{-6} \text{ m}) = 110$ channels.

But recall that the above calculation was for a repeating pitch up to but not including the last channel, so the number of channels available for cooling is $n = 111$.

(ii) Required flow rate of water (Answer: 0.00239 kg/s or 143.6 ml/min, total).

The inlet water temperature is given as 35°C , and the stated assumption is that the water temperature rise is limited to 10°C . The mass flow rate can be calculated using the properties of water at the average temperature of 40°C by using the equation $q = \dot{m}_t c_p \Delta T$; where q is the power dissipated from the chip, c_p is the specific heat of water at constant pressure, and ΔT is the temperature change of the water. The total mass flow rate is

$$\dot{m}_t = \frac{q}{c_p \Delta T} = 100 \text{ W} / (4179 \text{ J/kg K})(10 \text{ K}) = 0.00239 \text{ kg/s} = 143.6 \text{ ml/min}$$

and the mass flow rate in one channel is given by

$$\dot{m}_c = \frac{q}{n c_p \Delta T} = 21.6 \times 10^{-6} \text{ kg/s} = 1.3 \text{ mL/min}$$

(iii) Flow Reynolds number (Answer: $Re = 164.7$).

The flow Reynolds number using the mean water temperature (40°C) for fluid properties can be found using the hydraulic diameter D_h given by Eq. (3.7)

$$\begin{aligned} D_h &= \frac{2ab}{(a+b)} = 2(50 \times 10^{-6} \text{ m})(350 \times 10^{-6} \text{ m}) / (50 \times 10^{-6} \text{ m} + 350 \times 10^{-6} \text{ m}) \\ &= 87.5 \times 10^{-6} \text{ m} \end{aligned}$$

in the Reynolds number equation given by

$$\begin{aligned} Re &= \frac{\rho u_m D_h}{\mu} = \frac{\rho u_m A_c D_h}{A_c \mu} = \frac{\dot{m}_c D_h}{A_c \mu} \\ &= \frac{(21.6 \times 10^{-6} \text{ kg/s})(87.5 \times 10^{-6} \text{ m})}{(17.5 \times 10^{-9} \text{ m}^2)(655 \times 10^{-6} \text{ N s/m}^2)} = 164.7 \end{aligned}$$

This low Reynolds number clearly indicates laminar flow regime.

(iv) Fully developed assumption (Answer: fully developed assumption is valid—hydrodynamic entrance length = 0.72 mm and thermal entrance length = 6.25 mm).

The fully developed flow assumption is valid if the thermal and hydrodynamic entrance lengths are less than the channel length. For laminar flow, the hydrodynamic entrance length is given by Eq. (3.11) as

$$\begin{aligned} L_h &= 0.05ReD_h = 0.05(164.7)(87.5 \times 10^{-6} \text{ m}) = 720 \times 10^{-6} \text{ m} \\ &= 0.72 \text{ mm} \end{aligned}$$

and the thermal entrance length is given by Eq. (3.51) as

$$\begin{aligned} L_t &= 0.1RePrD_h = 0.1(164.7)(4.33)(87.5 \times 10^{-6} \text{ m}) = 6.24 \times 10^{-3} \text{ m} \\ &= 6.24 \text{ mm} \end{aligned}$$

Since the thermal and hydrodynamic entrance lengths are less than the channel length, the fully developed flow assumption is valid.

(v) Average heat transfer coefficient (Answer: $47.4 \times 10^3 \text{ W/m}^2 \text{ K}$).

Assumptions

- (1) Constant heat flux boundary condition.
- (2) Three-sided heating condition.

The Nusselt number using the thermal conductivity of water at the average temperature (40°C) is given by $Nu = hD_h/k$. A value for the fully developed Nusselt number can be obtained from Table 3.5 using the aspect ratio of the channel $\alpha_c = a/b = 1/7$. By linear interpolation, the Nusselt number is $Nu_{fd,3} = 6.567$.

The average heat transfer coefficient is

$$\bar{h} = \frac{kNu}{D_h} = (0.632 \text{ W/m K})(6.567)/(87.5 \times 10^{-6} \text{ m}) = 47.4 \times 10^3 \text{ W/m}^2 \text{ K}$$

(vi) Fin efficiency (Answer: 67%).

Assumptions

- (1) Adiabatic tip condition.

For an adiabatic tip, the fin efficiency equation is given by $\eta_f = \tanh(mb)/mb$ where b is the fin height

$$(350 \times 10^{-6} \text{ m}) \text{ and } m \text{ is defined as } m = (\bar{h}P/kA_c)^{1/2}$$

In the above equation, k is thermal conductivity of the fin material (given as $k = 180 \text{ W/m K}$), A_c is the cross-sectional area of the fin $L \times s = (0.01 \text{ m})(40 \times 10^{-6} \text{ m})$, and P is the perimeter of the fin which can be defined as $2L$ since the width of the fin is much smaller than its length. The term mb can be written as

$$\begin{aligned} mb &= \left(\frac{\bar{h}2L}{ksL}\right)^{1/2} b = \left(\frac{2\bar{h}}{ks}\right)^{1/2} b \\ &= \left(\frac{2(47.4 \times 10^3 \text{ W/m}^2 \text{ K})}{(180 \text{ W/m K})(40 \times 10^{-6} \text{ m})}\right)^{1/2} (350 \times 10^{-6} \text{ m}) = 1.270 \end{aligned}$$

Therefore, the fin efficiency can be calculated as $\eta_f = \tanh(1.270)/1.270 = 0.672 = 67\%$.

(vii) Inlet and outlet surface temperatures at the base of the fin (Answer: $T_{s,i} = 36.3^\circ\text{C}$ and $T_{s,o} = 48.6^\circ\text{C}$).

Assumptions

(1) The heat flux is constant over the chip surface.

The surface heat flux considering the fin efficiency is given by

$$\begin{aligned} q'' &= q/(2b\eta_f + a)nL \\ &= \frac{100 \text{ W}}{[2(350 \times 10^{-6} \text{ m})(0.672) + 50 \times 10^{-6} \text{ m}](111)(0.01 \text{ m})} \\ &= 173 \times 10^3 \text{ W/m}^2 \end{aligned}$$

The relationship between heat flux, heat transfer, and temperature difference is given by $q'' = h(T_s - T_f)$ where the subscripts s and f refer to the surface and fluid, respectively. The *local* heat transfer coefficients at the inlet and outlet of the microchannels are needed in order to compute the surface temperatures. Since the flow is developing at the entrance of the microchannel, [Tables 3.5 and 3.6](#) are used with the channel aspect ratio and x^* for the inlet, where x^* is defined by [Eq. \(3.53\)](#). The entrance of the channel is assumed to begin at $x = 0.1 \text{ mm}$ from the edge of the chip, so x^* is

$$x_{in}^* = \frac{0.1 \times 10^{-3} \text{ m}}{(87.5 \times 10^{-6} \text{ m})(164.7)(4.33)} = 1.603 \times 10^{-3}$$

Using a linear interpolation in [Table 3.5](#), the fully developed Nusselt numbers for three-sided and four-sided heating are found to be 6.567 and 6.273, respectively. The thermal entry region Nusselt number for four-sided heating is found using [Table 3.6](#) to be 18.42 for the inlet. [Equation \(3.54\)](#) is used to obtain the local Nusselt number at the entrance as

$$Nu_{x,3}(x^*, \alpha_c) = 18.42 \frac{6.567}{6.273} = 19.28$$

Alternatively, equations given in [Appendix A](#) may be used for interpolating values from [Tables 3.2, 3.5, and 3.6](#).

Using the thermal conductivity of water at the given inlet temperature (35°C), the local heat transfer coefficient at the inlet is found to be

$$h = \frac{kNu}{D_h} = (0.625 \text{ W/m K})(19.28)/87.5 \times 10^{-6} \text{ m} = 47.9 \times 10^3 \text{ W/m}^2 \text{ K}$$

Since the flow is fully developed at the outlet, the three-sided Nusselt number from [Table 3.5](#) is used with the thermal conductivity of water at the outlet temperature (45°C). The local heat transfer coefficient at the exit is found to be

$$h = \frac{kNu}{D_h} = (0.638 \text{ W/m K})(6.567)/87.5 \times 10^{-6} \text{ m} = 47.9 \times 10^3 \text{ W/m}^2 \text{ K}$$

Using the value of the heat flux obtained above, the local heat transfer coefficients, and the given inlet and outlet water temperatures, the surface temperatures at the base of the fin at the fluid inlet and outlet are

$$T_s = \frac{q''}{h} + T_f = > T_{s,i} = 36.3^{\circ}\text{C} \quad \text{and} \quad T_{s,o} = 48.6^{\circ}\text{C}$$

(viii) Pressure drop in microchannel core (Answer: 43.6 kPa).

Assumptions

- (1) The core of the microchannel includes pressure drop due to only frictional losses in the fully developed region and the loss due to the developing region.

Since the flow is fully developed at the exit, the pressure drop is defined by

$$\Delta p = \frac{2(fRe)\mu u_m L}{D_h^2} + K(\infty) \frac{\rho u_m^2}{2}$$

where $K(\infty)$ is the Hagenbach factor, which is defined by [Eq. \(3.18\)](#) as

$$K(\infty) = 0.6796 + 1.2197\alpha_c + 3.3089\alpha_c^2 + 9.5921\alpha_c^3 + 8.9089\alpha_c^4 + 2.9959\alpha_c^5 = 0.8969$$

The $f Re$ term is given by [Eq. \(3.10\)](#) as

$$fRe = 24(1 - 1.3553\alpha_c + 1.9467\alpha_c^2 - 1.7012\alpha_c^3 + 0.9564\alpha_c^4 - 0.2537\alpha_c^5) \\ = 20.2$$

The pressure drop in the core of the microchannel is given by [Eq. \(3.14\)](#) as

$$\Delta p = \frac{2(20.2)(655 \times 10^{-6} \text{ N s/m}^2)(1.24 \text{ m/s})(0.01 \text{ m})}{(87.5 \times 10^{-6} \text{ m})^2} \\ + (0.8969) \frac{(991.8 \text{ kg/m}^2)(1.24 \text{ m/s})^2}{2} = 43.6 \text{ kPa}$$

(ix) Total pressure drop (Answer: 45.0 kPa).

Assumptions

- (1) Reservoirs are large so the Area of the reservoir \gg the Area of microchannel.

The total pressure drop between the inlet and outlet manifolds would include the pressure drop calculated above (43.6 kPa) plus the minor losses at the entrance and exit.

The minor loss is defined by $\Delta p = K(\rho u_m^2/2)$ where K is a loss coefficient related to area changes at the entrance or exit. Taking the area ratio as zero, based on Assumption 1, for a laminar flow regime, the contraction and expansion loss coefficients K_c and K_e can be obtained from Figure 3.5B as $K_c = 0.8$ and $K_e = 1.0$.

The total pressure drop is obtained by

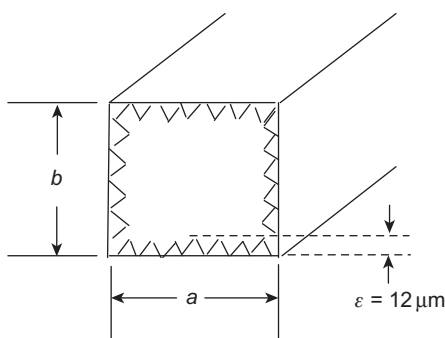
$$\Delta p = \frac{2(fRe)\mu u_m L}{D_h^2} + K(\infty) \frac{\rho u_m^2}{2} + K_c \frac{\rho u_m^2}{2} + K_e \frac{\rho u_m^2}{2} = 45.0 \text{ kPa}$$

The contraction and expansion coefficients were taken as the largest values on the chart in Figure 3.5B in order to design for the maximum expected pressure drop.

Example 3.2

A microchannel is etched in silicon. The microchannel surface is intentionally etched to provide an average roughness of $12 \mu\text{m}$. The microchannel dimensions measured from the root of the roughness elements are: width = $200 \mu\text{m}$, height = $200 \mu\text{m}$, length = 10 mm. Water flows through the microchannels at a temperature of 300 K. Calculate the core frictional pressure drop when (i) $m = 90 \times 10^{-6} \text{ kg/s}$, and (ii) $\dot{m} = 180 \times 10^{-6} \text{ kg/s}$.

Schematic



Solution

Properties: From Incropera et al. (2007), saturated water at 300 K: $\mu_f = 0.855 \times 10^{-3} \text{ N s/m}^2$, $\rho = 997 \text{ kg/m}^3$, $c_{p,f} = 4179 \text{ J/kg K}$, $k_f = 0.613 \text{ W/m K}$.

- (i) Core frictional pressure drop when $\dot{m} = 90 \times 10^{-6}$ kg/s
 (Answer: 29,365 Pa).

Calculate the hydraulic diameter using the constricted width (a_{cf}) and constricted height (b_{cf}) in Eq. (3.6)

$$D_{h,ci} = \frac{4A_c}{P_w} = a_{cf} = b_{cf} = 0.000176 \text{ m}$$

Calculate the Reynolds number of the fluid in a microchannel using Eq. (3.35):

$$Re_{cf} = \frac{\rho u_{m,cf} D_{h,cf}}{\mu} = \frac{(997.01 \text{ kg/m}^3)(2.91 \text{ m/s})(176 \times 10^{-6} \text{ m})}{(0.855 \times 10^{-3} \text{ N s/m}^2)} = 598$$

For fully developed laminar flow, the hydrodynamic entry length may be obtained using Eq. (3.11):

$$L_{h,cf} = 0.05 Re_{cf} D_{h,f} = 0.05(598)(0.176 \text{ mm}) = 5.26 \text{ mm}$$

Since $L > L_{h,cf}$, the fully developed flow assumption is valid.

The $f Re$ term can be obtained using Eq. (3.10):

$$\begin{aligned} fRe &= 24(1 - 1.3553\alpha_c + 1.9467\alpha_c^2 - 1.7012\alpha_c^3 + 0.9564\alpha_c^4 - 0.2537\alpha_c^5) \\ &= 14.23 \end{aligned}$$

The core frictional pressure drop can be calculated using Eq. (3.14):

$$\Delta p = \frac{2(fRe)\mu_{m,cf}L}{D_{h,cf}^2} + K(\infty) \frac{\rho u_{m,cf}^2}{2}$$

where $K(\infty)$ is given by Eq. (3.18).

$$\begin{aligned} K(\infty) &= (0.6796 + 1.219\alpha_c + 3.3089\alpha_c^2 - 9.5921\alpha_c^3 + 8.9089\alpha_c^4 - 2.9959\alpha_c^5) \\ &= 1.53 \end{aligned}$$

Hence

$$\begin{aligned} \Delta p &= \frac{2(14.23)(0.855 \times 10^{-3} \text{ N s/m}^2)(2.91 \text{ m/s})(0.01 \text{ m})}{(176 \times 10^{-6} \text{ m})^2} \\ &\quad + (1.53) \frac{(997.01 \text{ kg/m}^3)(2.91 \text{ m/s})^2}{2} = 29,356 \text{ Pa} \end{aligned}$$

- (ii) Core frictional pressure drop when $\dot{m} = 180 \times 10^{-6}$ kg/s
 (Answer: 68,694 Pa).

Calculate the Reynolds number of the fluid in a microchannel using Eq. (3.35):

$$Re_{cf} = \frac{\rho u_{m,cf} D_{h,cf}}{\mu} = \frac{(997.01 \text{ kg/m}^3)(5.83 \text{ m/s})(176 \times 10^{-6} \text{ m})}{(0.855 \times 10^{-3} \text{ N s/m}^2)} = 1200$$

For fully developed laminar flow, the hydrodynamic entry length may be obtained using Eq. (3.11):

$$L_{h,cf} = 0.05 Re_{cf} D_{h,cf} = 0.05(1200)(0.176 \text{ mm}) = 10.5 \text{ mm}$$

Since $L < L_{h,cf}$, the fully developed flow assumption is not valid.

Calculate the core frictional pressure drop with the developing laminar flow assumption. The apparent friction factor can be obtained from Table 3.2 using x^+ calculated from Eq. 3.16:

$$x^+ = \frac{x/D_h}{Re_{cf}} = \frac{0.01 \text{ m}}{(176 \times 10^{-6} \text{ m})(1200)} = 0.0475$$

From Table 3.2, $f_{app} Re = 21.35$, so the core frictional pressure drop can be calculated using the following equation:

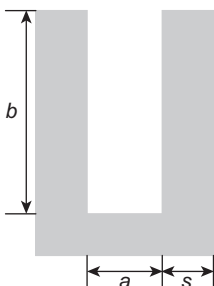
$$\begin{aligned} \Delta p &= \frac{2(f_{app} Re) \mu_{m,cf} L}{D_{h,cf}^2} \\ &= \frac{2(21.35)(0.855 \times 10^{-3} \text{ N s/m}^2)(5.83 \text{ m/s})(0.01 \text{ m})}{(176 \times 10^{-6} \text{ m})^2} = 68,694 \text{ Pa} \end{aligned}$$

Comments

- (1) The total frictional pressure drop has to consider the minor losses because the actual Δp is higher than the core frictional pressure drop.

Example 3.3

Consider a copper minichannel heat sink with an area of $30 \text{ mm} \times 30 \text{ mm}$ and relevant dimensions in Figure 3.14 with $a = 1 \text{ mm}$, $b = 3 \text{ mm}$, and $s = 1.5 \text{ mm}$. The heat dissipation is 100 W and the water inlet temperature is 30°C . The maximum surface temperature in the heat sink is limited to 80°C . Calculate the water flow rate under these conditions. Also calculate the frictional pressure drop in the core. Assume a constant heat transfer coefficient corresponding to fully developed conditions and take the thermal conductivity of copper to be 400 W/m K .



Assumptions

Laminar flow, constant heat flux equally distributed over the surface area, one-dimensional steady state conduction, and three-sided heated condition with an adiabatic tip for fin efficiency

$$a = 1 \text{ mm} = 10^{-3} \text{ m}, \quad b = 3 \text{ mm} = 3 \times 10^{-3} \text{ m}, \quad s = 1.5 \text{ mm} = 1.5 \times 10^{-3} \text{ m}, \\ w = L = 30 \times 10^{-3} \text{ m}, \quad T_{f,i} = 30^\circ\text{C}, \quad T_{s,o} = 80^\circ\text{C}, \quad q = 100 \text{ W}, \quad k_{\text{Cu}} = 400 \text{ W/m K}, \\ A_c = a \times b = 3 \times 10^{-6} \text{ m}^2, \quad \alpha_c = a/b = 1/3.$$

Solution

Equation (3.7) gives the hydraulic diameter:

$$D_h = \frac{2ab}{(a+b)} = \frac{2(10^{-3})(3 \times 10^{-3})}{(10^{-3} + 3 \times 10^{-3})} = 1.5 \times 10^{-3} \text{ m}$$

The Nusselt number can be obtained using Table 3.5 for a three-sided heated channel. Through interpolation this gives

$$Nu = Nu_{fd,3} = 5.224$$

For calculating water properties, let's assume the water exit temperature is equal to the maximum surface temperature of the heat sink. Then the average water temperature is

$$T_{\text{avg}} = (30^\circ\text{C} + 80^\circ\text{C})/2 = 55^\circ\text{C}$$

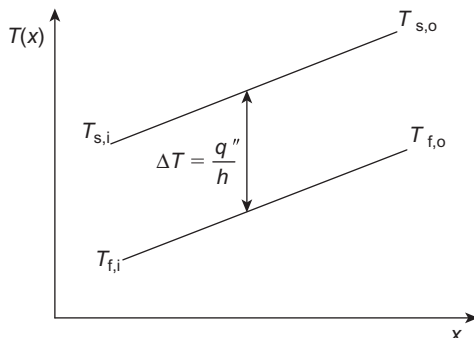
Properties of water at 55°C (from Incropera et al., 2007):

$$\rho = 985 \text{ kg/m}^3, \quad c_p = 4.183 \text{ kJ/kg K}, \quad \mu = 505 \times 10^{-6} \text{ kg/ms}, \quad k = 648 \times 10^{-3} \text{ W/m K}$$

The average heat transfer coefficient is calculated using the Nusselt number, which is rearranged to give

$$\bar{h} = \frac{kNu}{D_h} = \frac{(0.648)(5.224)}{(1.5 \times 10^{-3})} = 2.26 \times 10^3 \text{ W/m}^2 \text{ K}$$

By relating the conductive and convective heat transfer for a constant heat flux, the average temperature difference between the surface and the fluid is given as



$$\Delta T = \frac{q}{h(2b\eta_f + a)nL}$$

The number of channels is $n = (\text{overall width}/\text{channel} + \text{fin}) = (w/a + s) = (0.030/0.001 + 0.0015) = 12$

The fin efficiency is $\eta_f = (\tanh(mb)/mb)$

$$mb = \sqrt{\frac{2\bar{h}}{k_{\text{Cu}}s}} \quad b = \sqrt{\frac{2(2.26 \times 10^3)}{(400)(1.5 \times 10^{-3})}} \times (3 \times 10^{-3}) = 0.260$$

$$\eta_f = \frac{\tanh(0.260)}{(0.260)} = 0.978$$

$$\Delta T = \frac{100}{(2.26 \times 10^3)[2(3 \times 10^{-3})(0.978) + 10^{-3}(12)(30 \times 10^{-3})]} = 17.9^\circ\text{C}$$

The fluid outlet temperature is $T_{f,o} = T_{s,o} - \Delta T = 80^\circ\text{C} - 17.9^\circ\text{C} = 62.1^\circ\text{C}$

The average water temperature is $T_{\text{avg}} = (30^\circ\text{C} + 62.1^\circ\text{C})/2 = 46.1^\circ\text{C}$

T_{avg} is off by 9° . It is necessary to iterate again with the updated average temperature of 46°C .

Properties of water at 46°C (from Incropera et al., 2007):

$$\rho = 990 \text{ kg/m}^3, c_p = 4.180 \text{ kJ/kg K}, \mu = 588 \times 10^{-6} \text{ kg/ms}, \\ k = 639 \times 10^{-3} \text{ W/m K}$$

Following identical steps the new values are

$$\bar{h} = 2.23 \times 10^3 \text{ W/m}^2 \text{ K}, mb = 0.258, \eta_f = 0.978, \Delta T = 18.2^\circ\text{C}, T_{f,o} = 61.8^\circ\text{C}$$

$$T_{\text{avg}} = (30 + 61.8)/2 = 45.9^\circ\text{C}$$

The calculated average temperature is approximately the same as the assumed value. No more iterations are necessary.

$$T_{s,i} = T_{f,i} + \Delta T = 30^\circ\text{C} + 18.2^\circ\text{C} = 48.2^\circ\text{C}$$

$$q = \dot{m}c_p\Delta T_{\text{fluid}}$$

$$\dot{m}_t = \frac{q}{c_p\Delta T_{\text{fluid}}} = \frac{(100)}{(4180)(61.8 - 30)} = 752 \times 10^{-6} \text{ kg/s}$$

$$\dot{Q}_c = \frac{\dot{m}_t(1/n)}{\rho} = \frac{(752 \times 10^{-6})(1/2)}{(990)} = 63.3 \times 10^{-9} \text{ m}^3/\text{s} \quad \text{or} \quad 3.80 \text{ ml/min}$$

$$u_m = \frac{Q_c}{A_c} = \frac{(63.3 \times 10^{-9})}{(3 \times 10^{-6})} = 0.0211 \text{ m/s}$$

$$Re = \frac{D_h u_m \rho}{\mu} = \frac{(1.5 \times 10^{-3})(0.0211)(990)}{(588 \times 10^{-6})} = 53.3$$

Flow is laminar, so the original assumption is correct.

Equation (3.14) gives the pressure drop, $\Delta p = (2(fRe)\mu u_m L/D_h^2) + K(\infty)(\rho u_m^2/2)$

fRe can be determined with Eq. (3.10):

$$fRe = 24(1 - 1.3553\alpha_c + 1.9467\alpha_c^2 - 1.7012\alpha_c^3 + 0.9564\alpha_c^4 - 0.2537\alpha_c^5) = 17.1$$

Hagenbach's factor comes from Eq. (3.18):

$$K(\infty) = 0.6796 - 1.2197\alpha_c + 3.3089\alpha_c^2 - 9.5921\alpha_c^3 + 8.9089\alpha_c^4 - 2.9959\alpha_c^5 = 1.20$$

The pressure drop in the core is therefore

$$\Delta p = \frac{2(17.1)(588 \times 10^{-6})(0.0211)(30 \times 10^{-3})}{(1.5 \times 10^{-3})^2} + (1.20) \frac{(990)(0.0211)^2}{2} = 5.92 \text{ Pa}$$

We need to calculate the hydrodynamic and thermal entrance lengths to justify fully developed conditions.

Using Eq. (3.11) we have $L_h = 0.05$ $D_h Re = 0.05$ (1.5×10^{-3}) (53.3) $= 0.00400 \text{ m} = 4.00 \text{ mm}$.

Similarly, Eq. (3.51) gives $L_t = 0.05$ $D_h Re Pr = 0.05$ (1.5×10^{-3}) (53.3) (3.85) $= 0.0154 \text{ m} = 15.4 \text{ mm}$.

This validates the fully developed assumption as given in the problem statement.

Comments

If the heat dissipation is increased to 200 W, the flow rate will be 18.4 ml/min. This increases the pressure drop to 38.8 Pa. This illustrates the performance hit for increased heat dissipation and the need to develop microchannel cooling under turbulent conditions where the heat transfer coefficient will be larger. For turbulent flow more heat can be dissipated with minimal performance loss in pressure drop.

3.11 Practice problems

Problem 3.1

Solve Example 3.1 with copper as the substrate, with a thermal conductivity of 380 W/m K.

Problem 3.2

For [Example 3.1](#), plot the outlet surface temperature and pressure drop as a function of the channel depth b over a range of 200–600 μm .

Problem 3.3

For [Example 3.1](#), plot the outlet surface temperature and pressure drop as a function of the channel width a over a range of 50–200 μm .

Problem 3.4

Solve [Example 3.1](#) with a split-flow arrangement. Neglect the area reduction caused by the central manifold.

Problem 3.5

Solve [Example 3.1](#) with copper substrate and a split-flow arrangement. Assume the channel width to be 100 μm and a depth of 800 μm . Neglect the area reduction caused by the central manifold.

Problem 3.6

For [Example 3.3](#) with copper, plot the outlet surface temperature and the pressure drop as a function of the channel depth over a range of 200–2000 μm .

Problem 3.7

In [Example 3.3](#), redesign the heat sink if the design heat load increases to 500 W. You may have to rework the channel geometry and flow arrangements.

Problem 3.8

Design a microchannel heat exchanger to dissipate 800 watts from a copper heat sink of 20 mm \times 20 mm heated surface area. The inlet water temperature is 40°C, and the maximum surface temperature in the heat sink is desired to be below 60°C. Check your channel dimensions from a manufacturing standpoint (provide the manufacturing technique you will be implementing). Do not neglect the temperature drop occurring in the copper between the base of the channels and the bottom surface of the heat sink receiving heat. Show the details of the manifold design.

Problem 3.9

A copper minichannel heat sink has an area of $30\text{ mm} \times 30\text{ mm}$, and relevant dimensions in [Figure 3.14](#) are $a = 1\text{ mm}$, $b = 3\text{ mm}$, and $s = 1.5\text{ mm}$. Calculate the maximum heat dissipation possible with an inlet water temperature of 30°C and the maximum surface temperature in the heat sink limited to 80°C . Calculate the water flow rate under these conditions. Also calculate the frictional pressure drop in the core under these conditions.

Problem 3.10

Design a minichannel heat exchanger to dissipate 5 kW of heat from a copper plate with a footprint of $10\text{ cm} \times 12\text{ cm}$. The plate surface temperature should not exceed 60°C , and the inlet design temperature for water is 35°C . Calculate the water flow rate, outlet water temperature, and core frictional pressure drop. Compare the performance of (a) straight once-through flow passages and (b) split-flow passages.

Problem 3.11

Design the heat exchanger for [Problem 3.10](#) in aluminum, and compare its performance with a copper heat sink.

Appendix A**Table A.1** Curve-Fit Equations for [Tables 3.2, 3.5, and 3.6](#)

Equations	Constants					
	a	b	c	d	e	f
1	141.97	-7.0603	2603	1431.7	14364	-220.77
2	142.05	-5.4166	1481	1067.8	13177	-108.52
3	142.1	-7.3374	376.69	800.92	14010	-33.894
4	286.65	25.701	337.81	1091.5	26415	8.4098
5	8.2321	2.0263	1.2771	0.29805	2.2389	0.0065322
6	8.2313	1.9349	-2.295	0.92381	7.928	0.0033937
7	36.736	2254	17559	66172	555480	1212.6
8	30.354	1875.4	13842	154970	783440	-8015.1
9	31.297	2131.3	14867	144550	622440	-13297
10	28.315	3049	27038	472520	1783300	-35714
11	6.7702	-3.1702	0.4187	2.1555	2.76×10^{-6}	NA
12	9.1319	-3.7531	0.48222	2.5622	5.16×10^{-6}	NA

Equation form:

Equations 1–4: $y = (a + cx^{0.5} + ex/1 + bx^{0.5} + dx + fx^{1.5})$

Equations 5–10: $y = (a + cx + ex^2/1 + bx + dx^2 + fx^3)$

Equations 11–12: $y = a + bx + c(\ln x)^2 + d \ln x + ex^{-1.5}$

Equation variables:

Laminar flow friction factor in entrance region of rectangular ducts, [Table 3.2](#):

y -variable—friction factor

x -variable—Equation 1: $\alpha_c = 1.0$

Equation 2: $\alpha_c = 0.5$

Equation 3: $\alpha_c = 0.2$

Equation 4: $0.1 = \alpha_c = 10$

Fully developed Nusselt number for three-sided heating, [Table 3.5](#):

y -variable—Nusselt number for three-sided heating

x -variable—Equation 5: α_c

Fully developed Nusselt number for four-sided heating, [Table 3.5](#):

y -variable—Nusselt number for four-sided heating

x -variable—Equation 6: α_c

Thermal entry region Nusselt numbers for four-sided heating, [Table 3.6](#):

y -variable—Nusselt number for four-sided heating in the entry region

x -variable—Equation 7: $\alpha_c = 0.1$

Equation 8: $\alpha_c = 0.25$

Equation 9: $\alpha_c = 0.333$

Equation 10: $\alpha_c = 0.5$

Equation 11: $\alpha_c = 1.0$

Equation 12: $\alpha_c = 10$

References

- Adams, T.M., Abdel-Khalik, S.I., Jeter, M., Qureshi, Z.H., 1997. An experimental investigation of single-phase forced convection in microchannels. *Int. J. Heat Mass Transfer* 41 (6–7), 851–857.
- Akhavan-Behabadi, M.A., Kumar, R., Salimpour, M.R., Azimi, R., 2010. Pressure drop and heat transfer augmentation due to coiled wire inserts during laminar flow of oil inside a horizontal tube. *Int. J. Therm. Sci.* 49, 373–379.
- ASME Standard B46.1-2002. Surface Texture (Surface Roughness, Waviness, and Lay). The American Society of Mechanical Engineers, An American National Standard (ASME B46.1-2002), pp. 1–98.

- Baviere, R., Ayela, F., First local measurement in microchannels with integrated micromachined strain gauges. Paper No. ICMM2004-2406, Second International Conference on Microchannels and Minichannels, Rochester, NY, June 17–19 2004, pp. 221–228.
- Baviere, R., Ayela, F., Le Person, S., Favre-Marinet, M., An experimental study of water flow in smooth and rough rectangular microchannels. Paper No. ICMM2004-2338, Second International Conference on Microchannels and Minichannels, Rochester, NY, June 17–19 2004, pp. 221–228.
- Baviere, R., Gamrat, G., Favre-Marinet, M., Le Person, S., 2006. Modelling of laminar flows in rough-wall microchannels. *J. Fluids Eng.* 128 (4), 734–741.
- Bergles, A.E., Lienhard, J.H.V., Kendall, G.E., Griffith, P., 2003. Boiling and condensation in small diameter channels. *Heat Transfer Eng.* 24, 18–40.
- Bergman, T.L., 2009. Effect of reduced specific heats of nanofluids on single phase, laminar internal forced convection. *Int. J. Heat Mass Transfer* 52, 1240–1244.
- Brackbill, T.P., Kandlikar, S.G., 2010. Application of lubrication theory and study of roughness pitch during laminar, transition and low Reynolds number turbulent flow at microscale. *Heat Transfer Eng.* 31 (8), 635–645.
- Bucci, A., Celata, G.P., Cumo, M., Serra, E., Zummo, G., Water single-phase fluid flow and heat transfer in capillary tubes. Paper No. ICMM2004-2406, Second International Conference on Microchannels and Minichannels, Rochester, NY, 17–19 June 2004, pp. 221–228. International Conference on Microchannels and Minichannels. Paper # 1037, ASME, pp. 319–326.
- Celata, G.P., Cumo, M., Guglielmi, M., Zummo, G., 2002. Experimental investigation of hydraulic and single phase heat transfer in 0.130 mm capillary tube. *Micromechanics and Thermophys. Eng.* 6, 85–97.
- Chen, R.Y., 1972. Flow in the entrance region at low Reynolds numbers. *J. Fluids Eng.* 95, 153–158.
- Chein, R., Huang, G., 2005. Analysis of microchannel heat sink performance using nanofluids. *Appl. Therm. Eng.* 25, 3104–3114.
- Choi, S.U.S., 1995. Enhancing thermal conductivity of fluids with nanoparticles, In: Developments and applications of non-Newtonian flows, Singer, D.A., and Wang, H.P. (Eds), FED231, ASME, New York, NY.
- Colgan, E.G., Furman, B., Gaynes, M., Graham, W., LaBianca, N., Magerlein, J.H., et al., A practical implementation of silicon microchannel coolers for high power chips. Invited Paper presented at IEEE-Semi-Therm 21, San Jose, 15–17 March, 2005.
- Costaschuk, D., Elsnab, J., Petersen, S., Klewicki, J.C., Ameel, T., 2007. Axial static pressure measurements of water flow in a rectangular microchannel. *Exp. Fluids* 43, 907–916.
- Curr, R.M., Sharma, D., Tatchell, D.G., 1972. Numerical predictions of some three-dimensional boundary layers in ducts. *Comput. Method Appl. Mech. Eng.* 1, 143–158.
- Darcy, H., 1857. Recherches experimentales relatives au movement de L'Eau dans les Tuyaux. Mallet-Bachelier, Paris, France.
- Dharaiya, V.V., Kandlikar, S.G., 2012. Numerical investigation of heat transfer in rectangular microchannels under H2 boundary condition during developing and developed laminar flow. *J. Heat Transfer* 134 (2), 020911 (10 pages).
- Dharaiya, V.V., Kandlikar, S.G., 2013. A numerical study on the effects of 2d structured sinusoidal elements on fluid flow and heat transfer at microscale. *Int. J. Heat Mass Transfer* 57, 190–201.
- Fanning, T.A., 1886. Practical Treatise and Hydraulic and Water Supply Engineering. Van Nostrand (revised edition of 1877).
- Gad-el-Hak, M., 1999. The fluid mechanics of microdevices. *J. Fluids Eng.* 121, 7–33.

- Gamrat, G., Favre-Marinet, M., Asendrych, D., Numerical modeling of heat transfer in rectangular microchannels. Paper No. ICMM2004-2336, Second International Conference on Microchannels and Minichannels, 16–18 June 2004, Rochester, NY, pp. 205–212.
- Gamrat, G., Favre-Marinet, M., Le Person, L., Baviere, R., Ayela, F., 2008. An experimental study of roughness effects on laminar flow in microchannels. *J. Fluid Mech.* 594, 399–423.
- Garinella, S.V., Singhal, V., 2004. Single-phase flow and heat transport and pumping considerations in microchannel heat sinks. *Heat Transfer Eng.* 25 (1), 15–25.
- Ghajar, A.J., Tang, C.C., Cook, W.L., 2010. Experimental investigation of friction factor in the transition region for water flow in minitubes and microtubes. *Heat Transfer Eng.* 31 (8), 646–657.
- Gnielinski, V., 1976. New equations for heat and mass transfer in turbulent pipe and channel flow. *Int. Chem. Eng.* 16, 359–368.
- Guo, Z.-Y., Li, Z.-X., 2003. Size effect on single-phase channel flow and heat transfer at microscale. *Int. J. Heat Fluid Flow* 24, 284–298.
- Haaland, S.E., 1983. Simple and explicit formulas for the friction factor in turbulent flow. *J. Fluids Eng.* 105 (1), 89–90.
- Harpole, G., Eninger, J.E., Micro-channel heat exchanger optimization. Proceedings—IEEE Semiconductor Thermal and Temperature Measurement Symposium, February, 1991, pp. 59–63.
- Hartnett, J.P., Koh, J.C.Y., McComas, S.T., 1962. A comparison of predicted and measured friction factors for turbulent flow through rectangular ducts. *J. Heat Transfer* 84, 82–88.
- Hetsroni, G., Mosyak, A., Pogrebnyak, E., Yarin, L.P., 2005. Heat transfer in micro-channels: comparison of experiments with theory and numerical results. *Int. J. Heat Mass Transfer* 48, 5580–5601.
- Hornbeck, R.W., 1964. Laminar flow in the entrance region of a pipe. *Appl. Sci. Res.* 13, 224–232.
- Huang, Z.F., Nakayama, A., Yang, K., Yang, C., Liu, W., 2010. Enhancing heat transfer in the core flow by using porous medium insert in a tube. *Int. J. Heat Mass Transfer* 53, 1164–1174.
- Incropera, F.P., DeWitt, D.P., Bergman, T.L., Lavine, A.S., 2007. *Introduction to Heat Transfer*. John Wiley and Sons, Hoboken, NJ.
- Jones Jr., O.C., 1976. An improvement in the calculation of turbulent friction in rectangular ducts. *J. Fluids Eng.* 98, 173–181.
- Judy, J., Maynes, D., Webb, B.W., 2002. Characterization of frictional pressure drop for liquid flows through microchannels. *Int. J. Heat Mass Transfer* 45, 3477–3489.
- Jung, J.-Y., Oh, H.-S., Kwak, H.-Y., 2009. Forced convective heat transfer of nanofluids in microchannels. *Int. J. Heat Mass Transfer* 52, 466–472.
- Kakac, S., Shah, R.K., Aung, W., 1987. *Handbook of Single-Phase Convective Heat Transfer*. John Wiley and Sons, Inc., New York, NY.
- Kandlikar, S.G., 2005. High heat flux removal with microchannels—a roadmap of challenges and opportunities. *Heat Transfer Eng.* 26 (8).
- Kandlikar, S.G., Grande, W.J., 2004. Evaluation of single-phase flow in microchannels for high flux chip cooling—thermohydraulic performance enhancement and fabrication technology. *Heat Transfer Eng.* 25 (8), 5–16.
- Kandlikar, S.G., Upadhye, H.R., Extending the heat flux limit with enhanced microchannels in direct single-phase cooling of computer chips. Invited Paper presented at IEEE-Semi-Therm 21, San Jose, 15–17 March 2005.

- Kandlikar, S.G., Joshi, S., Tian, S., 2003. Effect of surface roughness on heat transfer and fluid flow characteristics at low Reynolds numbers in small diameter tubes. *Heat Transfer Eng.* 24 (3), 4–16.
- Kandlikar, S.G., Schmitt, D., Carrano, A.L., Taylor, J.B., 2005. Characterization of surface roughness effects on pressure drop in single-phase flow in minichannels. *Phys. Fluids* 17 (10), Available from: <http://dx.doi.org/10.1063/1.1896985>, Article Number: 100606.
- Kays, W.M., London, A.L., 1984. *Compact Heat Exchangers*. McGraw-Hill, New York, NY.
- Kishimoto, T., Sasaki, S., 1987. Cooling characteristics of diamond-shaped interrupted cooling fins for high power LSI devices. *Electron. Lett.* 23 (9), 456–457.
- Knight, R.W., Hall, D.J., Goodling, J.S., Jaeger, R.C., 1992. Heat sink optimization with application to microchannels. *IEEE Trans. Comp. Hybrids Manuf. Technol.* 15 (5), 832–842.
- Koo, J., Kleinstreuer, C., Analyses of liquid flow in micro-conduits. Paper No. ICMM2004-2334, Second International Conference on Microchannels and Minichannels, Rochester, NY, 17–19 June 2004a, pp. 191–198.
- Koo, J., Kleinstreuer, C., 2004b. Computational analysis of wall roughness effects for liquid flow in micro-conduits. *J. Fluids Eng.* 126 (1).
- Koo, J., Kleinstreuer, C., 2005. Laminar nanofluid flow in microheat-sinks. *Int. J. Heat Mass Transfer* 48, 2652–2661.
- Krishna, S.R., Pathipaka, G., Sivashanmugam, P., 2009. Heat transfer and pressure drop studies in a circular tube fitted with straight full twist. *Exp. Therm. Fluid Sci.* 33, 431–438.
- Lee, J., Mudawar, I., 2007. Assessment of the effectiveness of nanofluids for single-phase and two-phase heat transfer in microchannels. *Int. J. Heat Mass Transfer* 50, 452–463.
- Li, Z.X., Du, D.X., Guo, Z.Y. Experimental study on flow characteristics of liquid in circular microtubes. Proceeding of the International Conference on Heat Transfer and Transport Phenomena in Microscale, Banff, Canada, 15–20 October 2000, pp. 162–167.
- Lin, T.-Y., Kandlikar, S.G., 2012a. A theoretical model for axial conduction effects during single-phase flow in microchannels. *J. Heat Transfer* 134 (2), . Available from: <http://dx.doi.org/10.1115/1.4004936> Article Number: 020902 (6 pages).
- Lin, T.-Y., Kandlikar, S.G., 2012b. An experimental investigation of structured roughness effect on heat transfer during single-phase liquid flow at microscale. *J. Heat Transfer* 134 (10), Available from: <http://dx.doi.org/10.1115/1.4006844>, Article Number: 101701 (9 pages).
- Lin, T.-Y., Kandlikar, S.G., 2013a. Heat transfer investigation of air flow in microtubes I: effects of heat loss, viscous heating and axial conduction. *J. Heat Transfer* 135 (3), Available from: <http://dx.doi.org/10.1115/1.4007876031703> (9 pages).
- Lin, T.-Y., Kandlikar, S.G., 2013b. Heat transfer investigation of air flow in microtubes II: scale and axial conduction effects. *J. Heat Transfer* 135 (3), Available from: <http://dx.doi.org/10.1115/1.4007877031704> (6 pages).
- Maranzana, G., Perry, I., Maillet, D., 2004. Mini- and micro-channels: influence of axial conduction in the walls. *Int. J. Heat Mass Transfer* 47, 3993–4004.
- Mises, R. v., 1914. *Elemente der Technischen Hydrodynamik*. B. G. Teubner, Leipzig.
- Moody, L.F., 1944. Friction factors for pipe flow. *ASME Trans.* 66, 671–683.
- Niklas, M. Favre-Marinet, M., Pressure losses in a network of triangular minichannels. Paper No. ICMM2003-1039, First International Conference on Microchannels and Minichannels, 24–25 April 2003, pp. 335–350.

- Nikuradse, J., 1937. Stromungsgesetze in Rauen Rohren, VDI-Forschungsheft 361, Belige zu Forschung auf dem Gebiete des Ingenieurwesens Ausage B Band 4, July/August 1933. English Translation Laws of flow in rough pipes. NACA Tech. Mem. 1292.
- Phillips, R.J., 1987. Forced Convection, Liquid Cooled, Microchannel Heat Sinks (MS thesis). Department of Mechanical Engineering, Massachusetts Institute of Technology, Cambridge, MA.
- Phillips, R.J., 1990. Microchannel Heat Sinks, Advances in Thermal Modeling of Electronic Components and Systems. Hemisphere Publishing Corporation, New York, NY (Chapter 3).
- Ryu, J.H., Choi, D.H., Kim, S.J., 2002. Numerical optimization of the thermal performance of a microchannel heat sink. *Int. J. Heat Mass Transfer* 45, 2823–2827.
- Schmitt, D.J., Kandlikar, S.G., Effects of repeating microstructures on pressure drop in rectangular minichannels. Paper No. ICMM2005-75111, ASME, Third International Conference on Microchannels and Minichannels, Toronto, Canada, 13–15 June 2005.
- Shah, R.K., London, A.L., 1978. Laminar Flow Forced Convection in Ducts, Supplement 1 to Advances in Heat Transfer. Academic Press, New York, NY.
- Shen, P., Aliabadi, S.K., Abedi, J., A review of single-phase liquid flow and heat transfer in microchannels. Paper ICMM2004-2337, Second International Conference on Microchannels and Minichannels, 17–19 June 2004, pp. 213–220.
- Singh, P.K., Harikrishna, P.V., Sundarajan, T., Das, S.K., 2011. Experimental and numerical investigation into the heat transfer study of nanofluids in microchannel. *J. Heat Transfer* 133, 121701 (9 pages).
- Singh, P.K., Harikrishna, P.V., Sundarajan, T., Das, S.K., 2012. Experimental and numerical investigation into the hydrodynamics of nanofluids in microchannels. *Int. J. Heat Mass Transfer* 42, 174–186.
- Steinke, M.E., 2005. Characterization of Single-Phase Fluid Flow and Heat Transfer in Plain and Enhanced Silicon Microchannels (Ph.D. thesis). Microsystems Engineering, Rochester Institute of Technology, Rochester, NY.
- Steinke, M.E., Kandlikar, S.G., Single-phase enhancement techniques in microchannel flows. Paper No. ICMM2004-2328, Second International Conference on Microchannels and Minichannels, Rochester, NY, 17–19 June 2004a.
- Steinke, M.E., Kandlikar, S.G., 2004b. Review of single-phase heat transfer enhancement techniques for application in microchannels, minichannels and microdevices. *Int. J. Heat Technol.* 22 (2), 3–11.
- Steinke, M.E., Kandlikar, S.G., Single-phase liquid friction factors in microchannels. Paper No. ICMM2005-75112, Third International Conference on Microchannels and Minichannels, Toronto, Canada, 13–15 June 2005a.
- Steinke, M.E., Kandlikar, S.G., Review of single-phase liquid heat transfer in microchannels. Paper No. ICMM2005-75114, ASME, Third International Conference on Microchannels and Minichannels, Toronto, Canada, 13–15 June 2005b.
- Steinke, M.E., Kandlikar, S.G., Development of an experimental facility for investigating single-phase liquid flow in microchannels. Paper No. ICMM2005-75070, ASME, Third International Conference on Microchannels and Minichannels, Toronto, Canada, 13–15 June 2005c.
- Szewczyk, H., 2008. Entrance and end effects in liquid flow in smooth capillary tubes. *Chem. Process Eng.* 29, 979–996.

- Tiselj, I., Hetsroni, G., Mavko, B., Mosyak, A., Pogrebnyak, E., Segal, Z., 2004. Effect of axial conduction on the heat transfer in micro-channels. *Int. J. Heat Mass Transfer* 47, 2551–2565.
- Tu, X. and Hrnjak, P., Experimental investigation of single-phase flow and pressure drop through rectangular microchannels. ASME, ICMM2003-1028, First International Conference on Microchannels and Minichannels, 24–25 April 2003, pp. 257–267.
- Tuckerman, D.B., 1984. Heat Transfer Microstructures for Integrated Circuits (Ph.D. thesis). Stanford University, Stanford, CA.
- Tuckerman, D.B., Pease, R.F.W., 1981. High performance heat sink for VLSI. *IEEE Electron Dev. Lett.* 2 (5), 126–129.
- Wagner, R.N., Kandlikar, S.G., 2012. Effects of structures roughness on fluid flow at microscale level. *Heat Transfer Eng.* 33, 483–493.
- Webb, R.L., Eckert, E.R.G., Goldstein, R.J., 1971. Heat transfer and friction in tubes with repeated-rib roughness. *Int. J. Heat Mass Transfer* 14, 601–617.
- Wen, D.S., Ding, Y.L., 2004. Experimental investigation into convective heat transfer of nanofluids at the entrance region under laminar flow conditions. *Int. J. Heat Mass Transfer* 47 (24), 5181–5188.
- Wen, D.S., Ding, Y.L., 2005. Effect of particle migration on heat transfer in suspensions of nanoparticles flowing through minichannels. *Microfluid. Nanofluid.* 1, 183–189.
- Wibulswas, P., 1966. Laminar Flow Heat Transfer in Non-Circular Ducts (Ph.D. thesis). London University, London, UK.
- Wongcharree, K., Eiamsa-ard, S., 2011. Friction and heat transfer characteristics of laminar swirl flow through the round tubes inserted with alternate clockwise and counter-clockwise twisted-tapes. *Int. Commun. Heat Mass Transfer* 38, 348–352.
- Xiong, R., Chung, J., 2007. Flow characteristics of water in straight and serpentine micro-channels with miter bends. *Exp. Therm. Fluid Sci.* 31, 805–812.
- Xu, B., Ooi, K.T., Wong, N.T., Choi, W.K., 2000. Experimental investigation of flow friction for liquid flow in microchannels. *Int. Commun. Heat Mass Transfer* 27 (8), 1165–1176.
- Yang, C-Y., Lin, C-W., Lin, T-Y., Kandlikar, S.G., 2012. Heat transfer and friction characteristics of air flow in microtubes. *Exp. Therm. Fluid Sci.* 37, 12–18.
- Yu, D., Warrington, R., Barron, R., Ameel, T., 1995. An experimental investigation of fluid flow and heat transfer in microtubes. *Proc. ASME/JSME Therm. Eng. Conf.* 1, 523–530.